J. Fluid Mech. (2008), vol. 594, pp. 85–124. © 2008 Cambridge University Press
doi:10.1017/S0022112007008749 Printed in the United Kingdom

A computational parameter study for the three-dimensional shock–bubble interaction

JOHN H. J. NIEDERHAUS[1], J. A. GREENOUGH[2],
J. G. OAKLEY[1], D. RANJAN[1], M. H. ANDERSON[1]
AND R. BONAZZA[1]

[1]Department of Engineering Physics, University of Wisconsin-Madison, Madison, WI 53706, USA
[2]Lawrence Livermore National Laboratory, Livermore, CA 94550, USA

(Received 16 March 2007 and in revised form 17 August 2007)

The morphology and time-dependent integral properties of the multifluid compressible flow resulting from the shock–bubble interaction in a gas environment are investigated using a series of three-dimensional multifluid-Eulerian simulations. The bubble consists of a spherical gas volume of radius 2.54 cm (128 grid points), which is accelerated by a planar shock wave. Fourteen scenarios are considered: four gas pairings, including Atwood numbers $-0.8 < A < 0.7$, and shock strengths $1.1 < M \leqslant 5.0$. The data are queried at closely spaced time intervals to obtain the time-dependent volumetric compression, mean bubble fluid velocity, circulation and extent of mixing in the shocked-bubble flow. Scaling arguments based on various properties computed from one-dimensional gasdynamics are found to collapse the trends in these quantities successfully for fixed A. However, complex changes in the shock-wave refraction pattern introduce effects that do not scale across differing gas pairings, and for some scenarios with $A > 0.2$, three-dimensional (non-axisymmetric) effects become particularly significant in the total enstrophy at late times. A new model for the total velocity circulation is proposed, also based on properties derived from one-dimensional gasdynamics, which compares favourably with circulation data obtained from calculations, relative to existing models. The action of nonlinear-acoustic effects and primary and secondary vorticity production is depicted in sequenced visualizations of the density and vorticity fields, which indicate the significance of both secondary vorticity generation and turbulent effects, particularly for $M > 2$ and $A > 0.2$. Movies are available with the online version of the paper.

1. Introduction

Since the publication of the work of Rudinger & Somers (1960) on the shock–bubble interaction, it has been well-known that the interaction of a shock wave with a density inhomogeneity gives rise to perturbations that are absent under isentropic acceleration. These perturbations drastically alter the shape of both the inhomogeneity and the shock wavefront, and result in the formation of characteristic vortices and often of regions of intense mixing. In its simplest configuration – that of a planar shock wave propagating in a medium which is uniform except for a single spherical or cylindrical density inhomogeneity – this problem can be considered a 'building block' to a larger class of problems: shock-accelerated inhomogeneous flows, in which a shock wave propagates in a medium characterized by a distribution of inhomogeneities in density, temperature, or other state variables. Such flows are encountered in systems at wide-ranging energy and spatial scales, including shock propagation in the interstellar and intergalactic medium (see Klein, McKee & Colella 1994), sonic boom propagation (see Davy & Blackstock 1971), supersonic combustion (see Yang, Kubota & Zukoski 1994), shock mitigation in foams (see Delale, Nas & Tryggvason 2005), and shock-wave lithotripsy (see Jamaluddin, Ball & Leighton 2005). Further, viewed as a density-interface perturbation whose deformation is driven by an impulsive acceleration, the shock–bubble interaction has often been noted (see Haas & Sturtevant 1987) as a finite-mass high-interface-curvature analogue to the Richtmyer–Meshkov instability (see Richtmyer 1960; Meshkov 1970), which can arise as a significant limitation to the efficiency of ablatively driven compression in inertial confinement fusion implosions (see Lindl 1995).

1.1. *Description of the shock–bubble interaction*

The shock–bubble interaction is the unsteady flow that results from the passage of a shock wave across a discrete round inhomogeneity in an otherwise uniform medium. Here we consider the particular case of a planar incident shock wave and a discrete (sharply defined) spherical gas bubble in a gaseous environment. The ambient unshocked gas has density ρ_1 and sound speed c_1, and the unshocked bubble gas has density ρ_2 and sound speed c_2. Defining an Atwood number $A=(\rho_2-\rho_1)/(\rho_2+\rho_1)$, two situations are possible: $A<0$ (the 'light-bubble' case) and $A>0$ (the 'heavy-bubble' case). Zabusky & Zeng (1998) have differentiated these in terms of the change in the ideal-gas sound speed: for fixed uniform ratio of specific heats γ, $A<0$ implies $c_2>c_1$, and $A>0$ implies $c_2<c_1$. Thus, they refer to the light-bubble case as the 'slow-fast-slow' or 'SFS' case, and the heavy-bubble case as 'FSF'. The sign of A determines the configuration of the shock refraction patterns that develop in shock–bubble interactions. These patterns and the associated bubble deformation (figure 1) can be described in general terms as follows.

In both cases, the incident shock wave is refracted while crossing the curved upstream bubble surface, owing to the change in sound speeds. In light-bubble scenarios (depicted in figure 1(*a*, *b*), refraction is divergent, so that the transmitted shock wave has convex curvature. To maintain mechanical equilibrium at the interface, an upstream-directed reflected rarefaction arises in the ambient gas. The transmitted shock wave, in turn, generates an internally reflected shock wave at impact on the downstream interior bubble surface, which transits the bubble in the upstream direction. An irregular shock refraction pattern (see Henderson 1966, 1989) is formed outside the bubble as the transmitted shock wave propagates downstream, ahead of the exterior incident shock. This produces a Mach stem, triple point and precursor shock. A slip surface may also be traced in the flow along the path travelled by the triple point. Most importantly, vorticity is strongly deposited on the interface by the baroclinic mechanism (see Haas & Sturtevant 1987; Jacobs 1993) during shock transit, resulting in the inversion of the upstream portion of the interface and the formation of a vortex ring.

In the heavy-bubble scenario (figure 1*c*, *d*), refraction is convergent, so that the transmitted shock wave has concave curvature. In this case, mechanical equilibrium is maintained after shock impact by the generation of an upstream-directed reflected shock wave. The transmitted shock wave propagates across the bubble and generates an internally reflected rarefaction wave at impact on the downstream interior bubble surface. If the Atwood number (and thus the change in sound speeds) is high enough, portions of the shock front sweeping around the bubble periphery are diffracted (see Haas & Sturtevant 1987; Quirk & Karni 1996), meaning that they are turned toward

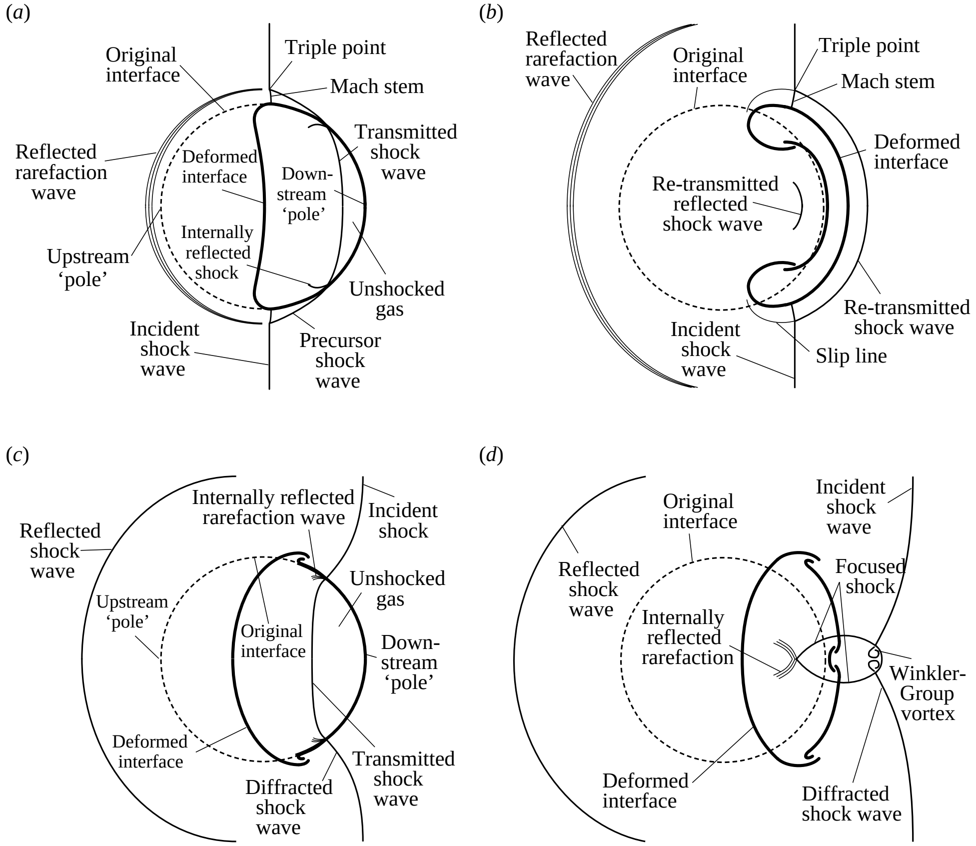

FIGURE 1. Representative schematic view of shock–bubble interaction flow field. Light-bubble ($A < 0$) scenario: (*a*) during initial shock wave transit, and (*b*) shortly after initial shock wave transit. Heavy-bubble ($A > 0$) scenario: (*c*) during initial shock wave transit, and (*d*) shortly after initial shock wave transit. Incident shock wave propagation is left-to-right.

the axis so that the surface of discontinuity remains nearly normal to the interface. These diffracted shock waves may then converge with the transmitted shock wave at the downstream pole, resulting in shock focusing and the propagation of secondary shock waves in the lateral and upstream directions. Vorticity is deposited baroclinically on the interface during the transit of the primary and secondary shocks, resulting in rotation primarily in an opposite sense to the light-bubble scenario. A supersonic vortex ring of the type depicted in the simulations of Winkler *et al.* (1987) also forms just behind the re-transmitted shock front in the ambient gas, and upstream- or downstream-oriented perturbations may develop at the downstream pole of the bubble.

It is important to note that the convergent or divergent nature of shock refraction patterns is determined by the acoustic impedance (ρc) mismatch at the interface. Hence, shock–bubble interactions will exhibit a divergent, 'light-bubble' refraction pattern in the non-uniform-γ case for $\rho_2 c_2/(\rho_1 c_1) < 1$, even if $A > 0$, and vice versa. It is therefore possible for externally reflected shock waves to appear in some cases with $A < 0$, if the change in the ratio of specific heat γ offsets the change in density. Conversely, externally reflected rarefaction waves may develop for $A > 0$. However, unusual cases such as these do not appear in the present study. For the scenarios considered here, $A < 0$ ('light-bubble') implies $\rho_2 c_2/(\rho_1 c_1) < 1$ and divergent refraction, and $A > 0$ ('heavy-bubble') implies $\rho_2 c_2/(\rho_1 c_1) > 1$ and convergent refraction.

1.2. *Overview of theoretical treatment*

In the literature, models have emerged for characterizing various aspects of this flow. A useful approach is to represent the bubble as a simple slab of the bubble gas, and use the well-known laws of one-dimensional gasdynamics (see Liepmann & Roshko 1957) to compute the changes in state variables after one or more shock reflection/transmission events at the slab surfaces. In this way, the effects of shock refraction and vorticity generation may be isolated from first-order effects. Giordano & Burtschell (2006) have used this approach to estimate the final total bubble volume, from the bulk gas density computed after a number of shock reflection/transmission events in the one-dimensional slab analogue.

In another useful type of approach, the total rotation introduced to the flow is characterized by calculating the velocity circulation on a half-plane in the flow. The most general approach of this type is the model of Samtaney & Zabusky (1994), which is based on scaling arguments arising from shock-polar analysis and observations from computational experiments analysing shock-wave interactions with planar interfaces. Also, the models of Picone *et al.* (1985) and Yang *et al.* (1994) can be equally useful. They are based on analytical approximations to baroclinic vorticity deposition. A new model for the circulation is proposed here, which predicts the circulation using line integrals in a reconstructed velocity field based on one-dimensional gasdynamics and scaling arguments derived from computational experiments. As an alternative, a simple formula based on normalized pressure differentials has been used successfully by Lee, Peng & Zabusky (2006) to predict the time rate of change in the circulation at intermediate times.

A third type of theoretical approach for shock–bubble interactions appearing in the literature is the use of dimensional analysis to obtain time-scaling parameters. This allows us to relate the rates of growth, acceleration, compression and other behaviour under varying initial conditions to the dimensional parameters that define the flow, by collapsing temporal trends for different scenarios on a single dimensionless time scale. Such an approach has been applied successfully in the experimental work of Layes (2005) and Ranjan *et al.* (2005), and in the numerical study of Klein *et al.* (1994). Following the analysis appearing in these three studies, the radius of the bubble is used as a characteristic length scale here, and time scales are constructed using the ratio of the radius to various characteristic velocity scales.

1.3. *Scope and plan for current numerical work*

In the present study, the purpose is twofold. First, the extensive database of two-dimensional simulations for the shock–bubble interaction (see Picone & Boris 1988; Klein *et al.* 1994; Zabusky & Zeng 1998; Marquina & Mulet 2003; Giordano & Burtschell 2006) is extended further, here, to three spatial dimensions. Such a study has been recommended (see Winkler *et al.* 1987; Klein *et al.* 1994; Zabusky & Zeng 1998) particularly as a means of characterizing the response of the shocked-bubble flow to fine-scale non-axisymmetric perturbations in the initial condition, and the growth of turbulence-like features. Secondly, a unified set of simulations is generated, which spans a significant portion of the parameter space of previous work on this problem, in order to facilitate the evaluation and continued development of analytical models and scaling laws for the integral properties of the shocked bubble flow field. The scope of the study is limited to the case of a spherical gas bubble, with grid-scale

Scenario number	Gas pair	M	A	χ	W_i (m s^{-1})	u'_1 (m s^{-1})	W_t (m s^{-1})
1	Air/He	1.20	−0.757	0.138	411.6	104.8	1112
2		1.50			514.5	238.3	1259
3		1.68			576.2	310.2	1344
4		3.00			1029	762.5	1958
5	N_2/Ar	1.33	0.176	1.426	463.9	168.1	432.3
6		2.88			1005	736.5	981.2
7		3.38			1179	896.8	1159
8	Air/Kr	1.20	0.486	2.892	411.6	104.8	275.4
9		1.50			514.5	238.3	361.7
10		1.68			576.2	310.2	414.8
11		3.00			1029	762.5	811.4
12	Air/R12	1.14	0.613	4.173	391.0	75.15	182.4
13		2.50			857.5	600.5	499.3
14		5.00			1715	1373	1080

TABLE 1. Parameter study overview, including the incident shock Mach number M, the Atwood number A and density ratio χ at the unshocked interface, and lab-frame speeds W_i, u'_1 and W_t of the incident shock wave, shocked ambient gas and transmitted shock wave, respectively.

initial perturbations, and particular emphasis is placed on heavy-bubble scenarios, for which a broader base of experimental data exists. Further, the study is limited to thermodynamic environments that are accessible to mechanical shock tubes operating with gas media initially at atmospheric conditions, thus, $A \leqslant 0.8$ and $M \leqslant 5$.

Fourteen scenarios, including four different gas pairings, are considered. An overview of the parameter study scenarios is given in table 1, showing the Mach number M of the incident shock wave, the Atwood number A and initial density ratio $\chi = \rho_2/\rho_1$ at the unshocked interface, and relevant velocities for each scenario, computed from the laws of one-dimensional gasdynamics. Scenarios are selected to coincide with previous experimental or computational work on this subject (see Layes, Jourdan & Houas 2003, 2005, Layes 2005; Layes & LeMétayer 2007; Ranjan *et al.* 2005, 2007; Zabusky & Zeng 1998). Although this produces a non-uniform sampling of the parameter space, the results may be referenced directly to previous work using only spatial scaling arguments if necessary. The direct comparison of experimental and numerical results, however, is beyond the scope of the present study, and will be undertaken in future work.

2. Governing equations and numerical method

2.1. *Euler equations*

Governing equations are obtained by considering the unsteady compressible flow of a single ideal fluid. If we neglect viscous effects (i.e restrict ourselves to short time scales), the flow is described by the three-dimensional compressible Euler equations. These can be formulated as a hyperbolic system of conservation laws which, in three-dimensional Cartesian space, takes the form

$$\frac{\partial U}{\partial t} + \frac{\partial F(U)}{\partial x} + \frac{\partial G(U)}{\partial y} + \frac{\partial H(U)}{\partial z} = 0, \tag{2.1}$$

where the conserved variables are $U = (\rho, \rho u, \rho v, \rho w, \rho E)^T$, and the fluxes are

$$F(U) = \begin{pmatrix} \rho u \\ \rho u^2 + p \\ \rho u v \\ \rho u w \\ \rho u E + u p \end{pmatrix}, \quad G(U) = \begin{pmatrix} \rho v \\ \rho v u \\ \rho v^2 + p \\ \rho v w \\ \rho v E + v p \end{pmatrix}, \quad H(U) = \begin{pmatrix} \rho w \\ \rho w u \\ \rho w v \\ \rho w^2 + p \\ \rho w E + w p \end{pmatrix}. \tag{2.2}$$

In this system, t, x, y and z are the time and space coordinates, and u, v, w, ρ, p and E represent the x-, y-, z-velocity, density, pressure and total energy per unit mass, respectively. In the perfect-gas idealization, the system is closed by introducing an explicit gamma-law equation of state,

$$p = (\gamma - 1)\rho \left[E - \tfrac{1}{2}(u^2 + v^2 + w^2)\right], \tag{2.3}$$

where γ is the ratio of specific heats and appears as a fluid property.

2.2. *Numerical method:* Raptor

Our purpose in the current work is to explore the parameter space of the shock–bubble interaction in three spatial dimensions. A second-order piecewise linear Eulerian Godunov code with adaptive mesh refinement (AMR), named *Raptor*, is chosen for this purpose, particularly for its excellent scalability. This code is based on the single-fluid compressible hydrodynamics code using block-structured AMR which was developed originally by the Center for Computational Sciences and Engineering at Lawrence Berkeley National Laboratory, and is currently under development by AX-Division at Lawrence Livermore National Laboratory. The scheme is a conservative finite-difference method; hence, mass, momentum and energy are all conserved. It is second-order accurate in space and time for smooth flow, and captures shock waves with minimal numerical dissipation and overshoot. Further, application of the scheme in simulations for shock-accelerated gas flows, e.g. by Henderson, Colella & Puckett (1991), has resulted in very good agreement with experiments.

The code is implemented in a hybrid C++/Fortran framework, where the infrastructure necessary for managing the AMR grid hierarchy and parallelization are implemented in C++ and the numerical integration kernels are implemented in Fortran, as described by Crutchfield & Welcome (1993). The current parallelization strategy for data distribution and load balancing are described by Rendleman *et al.* (1998), and the performance of the code on up to approximately 64 000 processors of the IBM BlueGene/L machine is described by Greenough *et al.* (2005).

2.3. *Adaptive mesh refinement*

The integration kernel is embedded within the block-structured AMR framework of Berger & Oliger (1984) in order to maximize resolution for fixed computational cost. This framework breaks the domain into a number of three-dimensional rectangular (‘block-structured’) grids, synchronizes the integration of (2.1) on each grid, and maintains a nested hierarchy of higher-resolution subgrids whose distribution is updated dynamically during the calculation to enhance spatial resolution and accuracy in regions of interest. The AMR technique has been used extensively in shock hydrodynamics computations (see Henderson *et al.* 1991; Klein *et al.* 1994), and its implementation has been discussed in detail by Berger & Colella (1989) and Bell, Colella & Trangenstein (1994).

2.4. *Eulerian Godunov method*

To summarize the scheme as implemented for the current study, numerical integration of the hyperbolic system (2.1) is accomplished using an operator-split second-order Godunov method. The basic kernel is the piecewise linear method (PLM) of Colella (1985), which is based on a higher-order extension of Godunov's method first proposed by van Leer (1979) – the MUSCL algorithm. In its one-dimensional form, cell-centred cell-averaged initial data $u(x_i, t_n)$ are interpolated using a piecewise-continuous linear profile, to obtain cell-edge values at the half-time step, $u(x_{i\pm 1/2}, t_{n+1/2})$. The profile slope is determined by a fourth-order finite-difference approximation, with constraints added to maintain monotonicity, which provides a profile that is steeper than that obtained by a standard fourth-order approximation. The resulting left and right states for the half-time step at each cell interface are then input to an approximate Riemann solver.

The solver is based on the ideas given in Bell *et al.* (1989), whereby one considers the cumulative effect of state changes across waves, and in Colella & Glaz (1985) whereby, to second order, rarefaction waves can be approximated as shock waves. The output from the Riemann solver, the so-called 'Godunov state,' is then used to compute the fluxes. The solution at the next time step $u(x_i, t_{n+1})$ is then obtained by explicit conservative differencing, with time-step size determined previously by the CFL condition. (By adopting a recursive time advancement approach, the solution is advanced on each AMR level using that level's appropriate CFL number.) The scheme is extended to two and three dimensions by Strang splitting (see Strang 1968), following the approach given by Bell *et al.* (1994), which yields second-order accuracy after the complete permutation cycle. Symmetry preservation tests of the three-dimensional integrator have been performed by running two-dimensional shock-contact interaction problems that are uniform in the third dimension of the domain. Results from x-y, y-z and x-z orientations are found to be identical to the level of round-off error.

2.5. *Multifluid capturing*

The single-fluid algorithm is generalized to treat multiple species by adopting a volume-of-fluid (VOF) multifluid approach following Miller & Puckett (1996), which allows multiple fluids with distinct equations of state for each material. In its original form, the VOF method tracks the material interface by performing a local interface reconstruction. The multifluid capturing method used in this study solves the same system of partial differential equations using the same numerical scheme as given in the above two references, but foregoes the local interface reconstruction, in favour of simple fluid volume advection (see Greenough *et al.* 1995). Mixed regions develop in the vicinity of fluid interfaces, but since individual species densities and energies are separately evolved, the mixing is not excessive when compared to other approaches given in the following test problem section.

3. Two-dimensional test problems

To verify the accuracy of the current method, two test problems in two spatial dimensions are simulated, which are drawn from well-known points of reference in the literature: one problem studied by Quirk & Karni (1996) (hereinafter referred to as QK), and the other by Zabusky & Zeng (1998) (hereinafter referred to as ZZ).

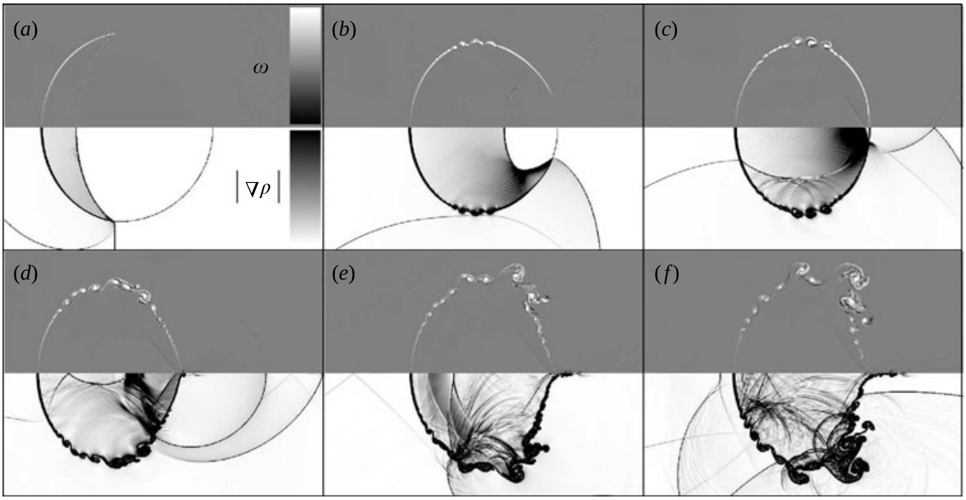

FIGURE 2. Vorticity magnitude (top) and density gradient magnitude (bottom) in the interaction of a $M = 1.22$ shock wave with a cylindrical R22 bubble of radius 2.5 cm, after Quirk & Karni (1996), simulated in two dimensions with *Raptor* at 446 grid points per bubble radius. Shock wave propagation is left-to-right. Times relative to initial shock wave impact: (*a*) 51 μs, (*b*) 142 μs, (*c*) 189 μs, (*d*) 247 μs, (*e*) 341 μs, (*f*) 412 μs.

3.1. *Cylindrical R22 bubble, shocked at* $M = 1.22$

In the first of these test problems, the shock–bubble interaction is considered for a cylindrical bubble of initial radius $R = 2.5$ cm, containing refrigerant gas R22 (molar mass $\mathscr{M} = 91.4\,\mathrm{g\,mol^{-1}}$, ratio of specific heats $\gamma = 1.249$), accelerated by a planar shock wave of strength $M = 1.22$ in air, as studied experimentally by Haas & Sturtevant (1987). QK integrated the Euler equations for this problem on a two-dimensional Cartesian mesh using a 'nearly conservative primitive-variable' shock-capturing scheme within a two-level AMR implementation, at an effective grid resolution of R_{446} (446 grid cells in a distance equal to R). The same initial and boundary conditions, AMR set-up and fluid properties are set up here – except that a smoothed initial bubble surface is created – and the Euler equations are integrated using the *Raptor* scheme described in § 2. In this 'smoothed' set-up, a subgrid VOF model (described in more detail in § 4.4) is used to smooth corners protruding from the curved bubble surface.

Plots of the vorticity magnitude $\omega = |\nabla \times \boldsymbol{V}|$ and the density gradient magnitude $|\nabla\rho|$ from these simulations are shown in figure 2, which can be compared to the images shown in figure 7(*a*, *c*–*e*, *g*, *h*) of QK, and to the experimental shadowgraphs in figure 11(*a*, *c*–*e*, *g*, *h*) of Haas & Sturtevant (1987). The flow visualizations in figure 2 demonstrate a qualitative level of agreement with the results of QK, for many of the features highlighted in that work, including the 'folding' of the transmitted shock wave seen in figure 2(*b*) ($t = 142$ μs), and the two-pronged axial jet arising owing to shock focusing, visible just right of centre in figure 2(*d*–*f*). The wave patterns associated with shock focusing and the convergence of diffracted and reflected shock waves observed both in Haas and Sturtevant's experiments and by QK at $t = 187$ μs and $t = 247$ μs are clearly resolved in the current simulations, as shown in figure 2(*c*, *d*). Further, the behaviour of the total velocity circulation over time, computed as $\Gamma(t) = \int \omega(x, y, t)\,\mathrm{d}A$, is shown in figure 3(*a*), and corresponds closely to the data

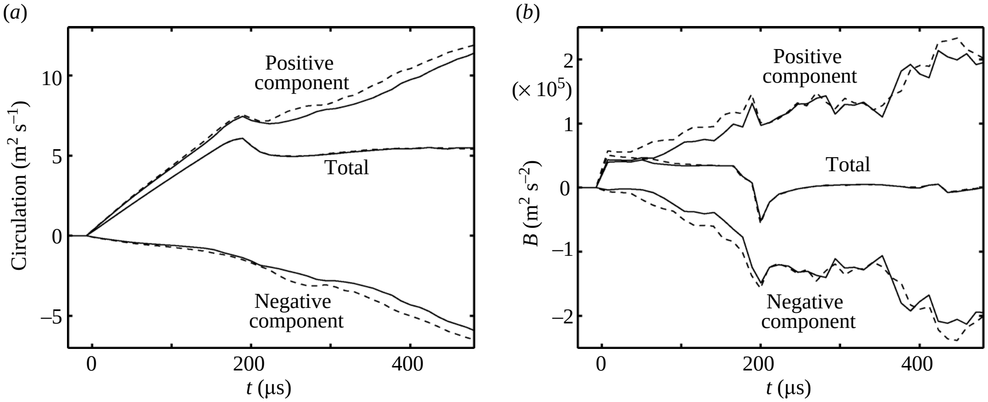

FIGURE 3. Decomposed (*a*) circulation Γ and (*b*) area-integrated baroclinic torque B versus time, for the interaction of an $M = 1.22$ shock wave with a cylindrical bubble of R22, with bubble surfaces 'unsmoothed' and discontinuous (- - -), or 'smoothed' (——) by use of a subgrid VOF technique.

shown in figure 15(*a*) of QK, with a peak circulation of 6.1 m^2 s^{-1} and a distinct drop in total circulation after shock passage, near $t = 188$ μs.

However, QK have noted that the initial development of vortical features on the surface of the bubble during shock passage has some grid-dependent properties. The growth of such grid-dependent features in Eulerian simulations for shock-contact initial-value problems has been characterized explicitly by Samtaney & Pullin (1996) as a manifestation of the non-convergence of Euler simulations. The effect of these features is particularly significant in the simulations described by QK, because of the discontinuous nature of the initial bubble surface. That is, the interfacial layer effectively has zero thickness, and the volume fraction f of the bubble-interior gas is everywhere either zero or one in the initial condition. Corrugations are therefore present on the surface, owing to the discretized projection of the curved interface onto the rectangular grid. This discretization sets a cutoff wavelength for the development of the Kelvin–Helmholtz roll-ups observed on the interface in figure 2, which results in the non-convergence of simulations for this flow using different methods and grid sizes. The 'smoothed' set-up has been introduced in order to minimize these effects, while keeping the density gradient at the bubble boundary as large as possible.

The calculations shown in figure 2 are repeated with an 'unsmoothed' definition of the initial bubble surface in which the subgrid smoothing in the initial condition is removed. The resulting post-shock growth of the positive and negative components of the circulation is enhanced up to roughly 10 % by $t = 100$ μs in the 'unsmoothed' case, relative to the 'smoothed' case, as shown in figure 3(*a*). The total circulation is unchanged, however, indicating that this is a more appropriate quantity for comparison between methods and initial data than the components of the circulation. The additional rotation manifested in the components of the circulation appears visibly as vortices on the interface in the 'unsmoothed' case, and is introduced by the same baroclinic mechanism (noted by subscript *b*) that is responsible for the large-scale vortical growth:

$$B(t) \equiv \left(\frac{\mathrm{d}\Gamma}{\mathrm{d}t}\right)_{\mathrm{b}} = \int \frac{1}{\rho^2}\left(\nabla\rho \times \nabla p\right) \cdot \mathrm{d}\boldsymbol{A}. \tag{3.1}$$

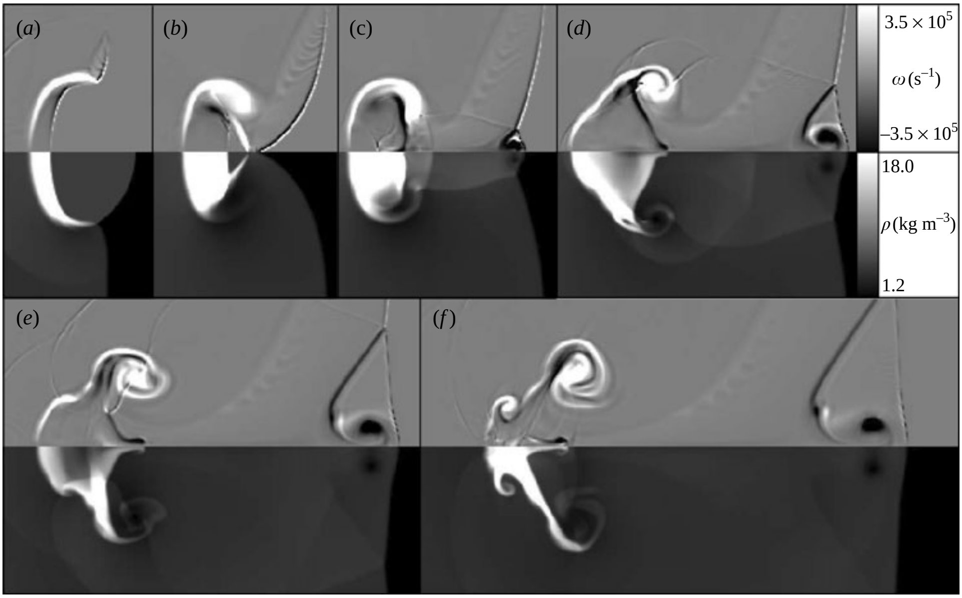

FIGURE 4. Vorticity magnitude (top) and density (bottom) plots for the interaction of an $M = 2.5$ shock wave with a spherical R12 bubble of radius 1 cm (after Zabusky & Zeng 1998), simulated with *Raptor* in two dimensions ((r, z)-symmetry) with 55 grid points per bubble radius. Shock wave propagation is left-to-right. Times relative to shock-wave impact: (*a*) 19 μs, (*b*) 34 μs, (*c*) 45 μs, (*d*) 60 μs, (*e*) 76 μs, (*f*) 93 μs.

The total area-integrated baroclinic torque $B(t)$, along with its positive and negative components, is plotted against time in figure 3(*b*), showing that, although the net or 'total' values of $B(t)$ are unchanged, the positive and negative components of B are both enhanced by as much as 40% during shock passage over the bubble in the 'unsmoothed' case, relative to the 'smoothed' case. (For example, at $t = 65$ μs, the positive component of baroclinic torque for the 'unsmoothed' case is $0.72 \times 10^5\ \mathrm{m}^2\ \mathrm{s}^{-2}$, while for the 'smoothed' case, it is only $0.46 \times 10^5\ \mathrm{m}^2\ \mathrm{s}^{-2}$.) Angular momentum added by this additional local torque accumulates over time, resulting in the enhanced magnitudes of the circulation components seen at late times in figure 3(*a*). The additional local baroclinic torque due to corners on the initial interface can have either sign, and thus adds nothing to the net integrated torque. However, the components of the local torque are significantly enhanced, resulting in the development of spurious vortices.

3.2. *Spherical R*12 *bubble, shocked at* $M = 2.5$

A second two-dimensional test problem for the shock–bubble interaction involves a spherical bubble of refrigerant gas R12 ($\mathscr{M} = 120.9\ \mathrm{g\,mol}^{-1}$, $\gamma = 1.141$) accelerated by an $M = 2.5$ planar shock wave. This scenario was simulated in ZZ on a uniform two-dimensional rectangular grid in (r, z)-symmetry about the direction of shock-wave motion, at a spatial resolution of R_{55}, using a second-order upwind TVD scheme. The flow is simulated with *Raptor*, using the same boundary and initial conditions and fluid properties as given by ZZ (including a 'smoothed' initial bubble surface), except that the geometry is scaled to a bubble radius of $R = 1$ cm here. In figure 4, the vorticity magnitude and density fields resulting from the *Raptor* simulation are plotted, showing the generation of opposite-signed vorticity and the emergence of

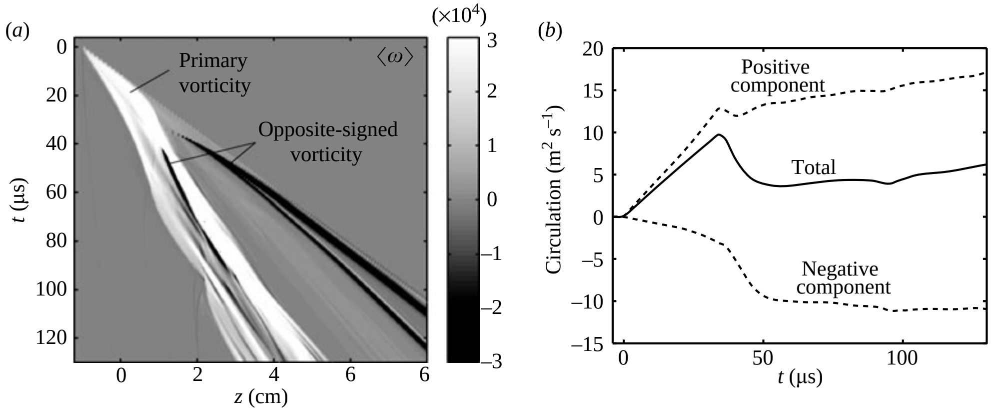

FIGURE 5. Integrated vortical behaviour for an $M = 2.5$, air–R12 shock–bubble interaction: (*a*) space–time plot of the r-integrated vorticity $\langle\omega\rangle$, after figure 16(*a*) of Zabusky & Zeng (1998), and (*b*) decomposed circulation in the domain versus time. Opposite-signed vorticity (black) begins to appear in (*a*) when the transmitted shock wave reflects from the downstream bubble surface, resulting in the downturn in circulation seen in (*b*) after $t = 34\,\mu\mathrm{s}$.

secondary vortical features at late times, as seen in figure 13 of ZZ. In particular, at $t = 93$ μs (figure 4*f*), we note the formation of a distinct secondary vortex ring on the upstream bubble surface, a small axial jet and vortex ring on the downstream surface and regions of opposite-signed vorticity within the primary vortex ring, as observed by ZZ. Very good qualitative agreement between the two methods is also evident, by comparison to ZZ.

These phenomena are depicted clearly in the plot of r-integrated vorticity in figure 5(*a*), in which figure 16(*a*) of ZZ is reproduced using the current results. The radially averaged vorticity $\langle\omega\rangle = (\int_0^{r_{max}} |\boldsymbol{\omega}|\mathrm{d}r)/r_{max}$ is plotted on the $(z,\, t)$-coordinate axes, with time progressing in the downward direction. The prominent white streak represents primary (positive) vorticity generated during initial shock passage. Black streaks appear amidst the white when the transmitted shock wave reaches $z = R$ (where the origin is at the bubble centre), owing to opposite-signed vorticity generated by reflected shock waves originating at that time. A prominent black streak runs ahead of the primary white structure, which represents the strong opposite-signed vorticity associated with the Winkler-Group supersonic vortex ring (see Winkler *et al.* 1987) trailing behind the shock wave after re-transmission into the ambient gas, first visible in figure 4(*c*) and depicted schematically in figure 1(*d*).

The circulation, integrated over the entire computational domain, and decomposed into its positive and negative components, is plotted over time in figure 5(*b*), which can be compared to figure 17(*c*) in ZZ. The total circulation has a peak at shock passage near $t = 34\,\mu\mathrm{s}$, followed by a very strong decrease to less than half the peak value. This abrupt decrease is caused by the deposition of opposite-signed vorticity by reflected shocks, and is vividly documented by ZZ. The plots in figure 5 demonstrate a high degree of quantitative agreement between the results of ZZ and results generated using *Raptor*.

4. Three-dimensional problem set-up

The extension from two-dimensional to three-dimensional treatment in this study is motivated by two observations: first, that the shock–bubble interaction exhibits

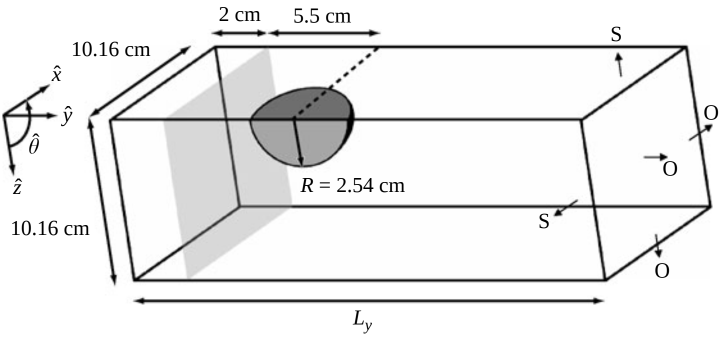

FIGURE 6. Schematic representation of initial and boundary conditions. Boundaries are symmetric (indicated by 'S') or outflow ('O'). The shock wave and free-stream flow move in the $+y$-direction.

features that are fundamentally turbulent (see Haas & Sturtevant 1987); and, secondly, that the behaviour of two-dimensional and three-dimensional turbulence is fundamentally different, owing to the absence of the vortex-stretching mechanism in two dimensions (see Pope 2000). Further, the presence of non-axisymmetric perturbations in the initial bubble geometry has been experimentally observed (see Klein *et al.* 2003) to initiate azimuthal vortex-ring instabilities of the type described for incompressible flows by Widnall, Bliss & Tsai (1974). These significant non-axisymmetric and turbulent effects arise because of the transport of mass, momentum and energy in the azimuthal direction, and lead to a late-time flow field characterized by disorderly motion and well-developed mixing regions, rather than by the well-defined coherent vortex dipoles and vortex projectiles observed in the two-dimensional simulations of ZZ.

4.1. *Computational mesh*

Three-dimensional calculations for the parameter study are set up on a Cartesian mesh subtending a quadrant of a typical shock tube flow field, including a quarter-spherical bubble of radius R (figure 6). (The growth of azimuthal mode numbers of less than four is thus excluded, and the computational effort here is devoted to the behaviour of shorter-wavelength perturbations.) A coordinate system is defined whose y-axis is coincident with the shock-tube long axis in the direction of shock-wave motion, and whose x- and z-axes run in the transverse directions. The incident shock wave and free-stream flow move in the $+y$-direction. The domain represents a physical space of dimensions $4R \times\ L_y, \times 4R$, where $4R = 10.16$ cm, and L_y is variable and selected to be large enough to accommodate the motion of the shocked bubble through the times of interest. An alternate coordinate system can be used to describe this space by defining an (x, z)-plane radial coordinate $\boldsymbol{r} = (x, 0, z)$ and an azimuthal unit vector $\hat{\theta} = \hat{y} \times \boldsymbol{r}/|\boldsymbol{r}|$.

In the present computations, the base grid resolution is $32 \times N_y \times 32$, where $N_y = L_y/\Delta_c$ and Δ_c is the (uniform) coarse-grid cell size. Two levels of AMR are superposed on the coarse grid, with a refinement ratio of 4 each. This gives a mesh resolution on the finest AMR level of $\Delta_f = 198\,\mu\text{m}$, which effectively corresponds to R_{128}. AMR settings are chosen to require maximum refinement in all regions having a non-zero bubble fluid volume fraction, and near any strong density gradients. Thus, the entire bubble region is captured with maximum resolution and accuracy, and the primary shock wave is captured at maximum resolution and accuracy from

Gas	$\mathscr{M}$ (g mol^{-1})	γ	c (m s^{-1})	ρ (kg m^3)
He	4.003	1.667	1007.2	0.167
N_2	28.013	1.399	348.8	1.165
Air	28.967	1.399	343.0	1.205
Ar	39.948	1.670	319.1	1.661
Kr	83.804	1.672	220.5	3.485
R12	120.91	1.143	151.8	5.028

TABLE 2. Initial properties of fluids present in the current calculations. The initial pressure and temperature in the system are 1.013×10^5 Pa and 300 K, respectively.

the initialization of the problem until refinement of density gradients is turned off after the shock wave has moved to a distance of at least $7R$ downstream from the bubble. In many cases, however, density-gradient refinement is enforced for twice that duration or more, to allow for replanarization of the shock front, particularly at high M and high A. Refinement of non-zero bubble fluid concentrations remains active throughout the entire calculation.

4.2. *Boundary conditions*

Symmetry boundary conditions are imposed on the two interior bounding surfaces parallel to the free-stream flow ($-\hat{x}$ and $-\hat{z}$), indicated by 'S' in figure 6. For a surface defined by outward normal vector $\hat{n}$, and velocity components parallel and perpendicular to the surface, $V_{\|}$ and $V_{\perp}$ respectively, the symmetry condition requires $V_{\perp}=0$, $\partial V_{\|}/\partial \hat{n}=0$, $\partial \rho/\partial \hat{n}=0$ and $\partial \rho E/\partial \hat{n}=0$. Outflow conditions are enforced on the four other bounding surfaces: two exterior surfaces parallel to the free-stream flow ($+\hat{x}$ and $+\hat{z}$), and two bounding surfaces normal to the mean flow ($-\hat{y}$ and $+\hat{y}$), denoted by 'O' in figure 6. The outflow condition applies a zeroth-order extrapolation to the boundary: i.e. the outermost plane of data is copied into the boundary, so that gradients across the boundary are zero. Shock reflections are then minimized, though not eliminated completely for flows with strong shock waves. Contamination of the solution by reflections in these cases is prevented by using adaptive gridding to keep the boundary as far from the region of interest as possible.

4.3. *Initial condition and fluid properties*

In the initial condition, a planar shock wave approaches a quarter-spherical bubble of a specified test gas, with radius $R=2.54$ cm, as shown in figure 6. The bubble interior gas (fluid 2) and unshocked ambient gas (fluid 1) are initialized at a pressure $p_1=p_2=101.3$ kPa and a temperature of $T_1=T_2=293$ K. The bubble and unshocked ambient gas are initially assumed to be at rest and in thermal and mechanical equilibrium, and any initial buoyant motion of the bubble is neglected here. The ratio of specific heats γ for each gas is obtained from JANAF data (see Gordon & McBride 1976), using the initial, unshocked pressure and temperature. Each fluid defined in the initial condition retains this fixed value of γ throughout the entire calculation. The bubble interior gases used in this study include helium, argon, krypton and dichlorodifluoromethane (refrigerant gas freon-12; hereinafter referred to as R12); the ambient gases used are air and nitrogen. (Nitrogen is used as the ambient gas in three scenarios in order to coincide with Ranjan *et al.* 2005.) The fixed fluid properties and initial densities and sound speeds for all of the gases used in the present parameter study can be found in table 2. Post-shock properties of the ambient gases used in the initialization are computed using the laws of one-dimensional gasdynamics (see Liepmann & Roshko 1957).

4.4. *Ill-posed phenomena and interface smoothing*

Using these initial data, then, the hyperbolic system of (2.1) is solved numerically as an initial-value problem. Samtaney & Pullin (1996) have thoroughly examined the issue of convergence for solutions of the compressible Euler equations, and shown that such calculations exhibit many ill-posed phenomena, the most significant of which is non-convergence of the solution at fixed time, with respect to the spatial-temporal resolution. This is a significant issue in the Eulerian calculations for shock-accelerated inhomogeneous flows, particularly in the absence of surface tension on fluid interfaces, and on rectangular grids. The solution does not always vary continuously with the initial data: interface features associated with projection onto a rectangular grid introduce grid-dependent features to shock refraction and vortex formation patterns, as discussed in § 3.1. The problem studied here may therefore be considered ill-posed, and in this sense, some small-scale features of the simulated flow fields may be suspect. However, the Eulerian AMR calculations discussed here represent the optimal computational effort for which solutions at this local resolution can be obtained in the context of a parameter study.

The effects of ill-posed phenomena in the results are minimized here by smoothing the initial bubble surface while maintaining its large density gradient. A subgrid VOF technique (mentioned in § 3.1) is used to ensure that the interfacial transition layer has a small but finite thickness. In this technique, each cell spanning the surface $(x^2+(y-y_c)^2+z^2)^{1/2}=R$ is first divided uniformly into 1000 subcells (ten in each direction), where y_c is the y-coordinate of the bubble centre. Each subcell is regarded as interior to the bubble if the bubble radius R exceeds the distance of the subcell centre to the bubble centre. The appropriate bubble fluid volume fraction for the parent cell is then determined by the number of interior subcells it subtends. This suppresses the appearance of corners on the bubble surface and produces a smoothed initial interface, with a maximum interfacial layer thickness of two grid cells, or $R/64$. Therefore, the effective perturbation on the initial bubble interface due to the grid has an amplitude of the order of $\Delta_f/10$ (19.8 µm, thus subgrid), and a wavelength of the order of Δ_f (198 µm).

5. Visualized flow fields

With this computational set-up, simulations are carried out for each of the 14 scenarios outlined in § 1 and table 1, using the *Raptor* code described in § 2. Data files are generated and stored after every fifth coarse-grid time step. The solution in each case is carried out to about $\tau=25$ (roughly 550 coarse-grid time steps, for these simulations), where τ is a dimensionless time scale based on, for each scenario, the greater of two speeds: the incident shock-wave speed W_i, or the speed of the transmitted shock wave W_t, computed from one-dimensional gasdynamics. Thus, for $A<0$, the transmitted shock wave is the fastest-moving shock wave in the system, and the dimensionless time scale τ is given by $\tau=tW_t/R$. This time scale can be computed in general as $\tau=tW^*/R$, where

$$W^* = \begin{cases} W_i, & A \geqslant 0, \\ W_t, & A < 0. \end{cases} \tag{5.1}$$

Under this time-scaling, in the absence of shock diffraction, the moment of shock passage (arrival of the first shock wave at the downstream bubble pole) corresponds to $\tau = 2$ for all scenarios. At shock passage, the initial stage of baroclinic vorticity deposition ceases, and opposite-signed vorticity appears as reflected shock and rarefaction waves transit the bubble.

Figures 7 to 10 show the development of the shocked bubble to $\tau = 25$, for four scenarios from the present simulations. In these representative plots, a slice is taken through the three-dimensional data at an angle of $\theta = \pi/6$ to the $x = 0$ plane. The total density ρ and vorticity magnitude $\omega = \boldsymbol{\omega} \cdot \hat{\theta}$ on the slice are plotted, where $\hat{\theta} = \hat{y} \times \hat{r} = (\cos(\theta), 0, -\sin(\theta))$, and $\hat{\theta}$ is directed normally out of the page on the top, and into the page on the bottom. The scenarios are arranged in figures 7 to 10 in order of increasing Atwood number. Individual frames are labelled by the dimensionless time τ, as given in the figure captions. These scenarios are also depicted in four movies available with the online version of the paper.

In these simulations, we consider the shock–bubble interaction within an idealized shock-tube environment. Thus, the incident shock wave is assumed to have negligible curvature, thickness and pressure decay, and the effects of radiation, conduction, phase changes, ionization, electric and magnetic fields and chemical and nuclear reactions (which are significant in many environments where shock–bubble interactions take place) are all neglected. The physical mechanisms that remain are purely hydrodynamic, and are dominated by three nonlinearly coupled, simultaneous processes: (i) shock-induced compression and heating; (ii) nonlinear-acoustic phenomena; and (iii) vorticity production and transport. The first of these can be clearly understood in terms of the Rankine–Hugoniot conditions, which characterize irreversible changes across surfaces of discontinuity in a gas. The second and third types of process are much more difficult to characterize, because they involve the highly nonlinear effects of the curved density interface at the bubble surface. This curvature leads to the 'scattering' of the incident shock wave into reflected, refracted, diffracted and transmitted waves (see Haas & Sturtevant 1987), collectively referred to as 'nonlinear-acoustic effects'. It also leads to the creation of a field of strong coupled vortices in the flow as the incident and scattered shock waves interact with the deforming density interface, via the baroclinic mechanism of (3.1). These two types of process are clearly visualized in figures 7 to 10, and described below.

5.1. *Shock refraction, reflection and diffraction*

Let us examine the scattered wave patterns seen in figures 7 to 10. The variety of refraction, reflection and diffraction patterns indicates the breadth of this parameter space. In the air–helium ($A = -0.757$) scenario shown in figure 7, it is apparent that the interaction has reached the irregular refraction stage by $\tau = 1.4$. Because of the very large negative Atwood number and the increase in sound speed across the bubble surface, the transmitted shock wave, indicated in figure 7(*a*), has distinctly convex curvature. Further, because of the small critical angle at this A, a precursor shock wave and Mach stem form outside the bubble, while the transmitted shock wave runs far ahead of the incident shock (figure 7*a*) inside the bubble. The bubble thus acts as a strongly divergent lens, refracting the shock front away from the axis.

In the nitrogen–argon ($A = 0.176$) scenario shown in figure 8, the refractive effect is very weak, owing to small A (see table 1). Thus, the transmitted shock wave has only very subtle concave curvature, even at $M = 3.38$ (figure 8*a*). In the air–krypton and air–R12 cases in figures 9 and 10, however, the refractive effect is quite strong. The formation of a collapsing shock cavity of the type described by ZZ is clearly

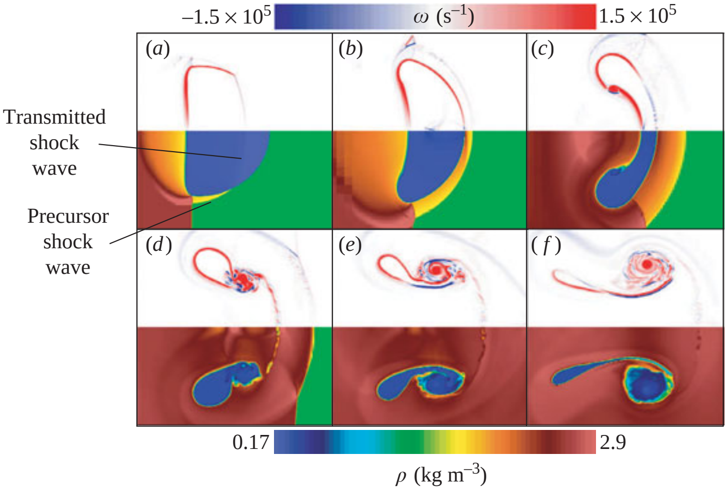

FIGURE 7. Density (bottom) and vorticity magnitude (top) on the $\theta=\pi/6$ plane for the $M=1.68$ air–He scenario ($A=-0.757$): (a) $\tau=1.4$, (b) $\tau=2.6$, (c) $\tau=5.2$, (d) $\tau=9.9$, (e) $\tau=15.0$, (f) $\tau=24.9$. The density colour palette is shown at the bottom, and vorticity is plotted on a symmetric colour palette centred on white, shown at the top. Note that $\tau=tW_t/R$ here. Incident shock wave propagation is left-to-right.

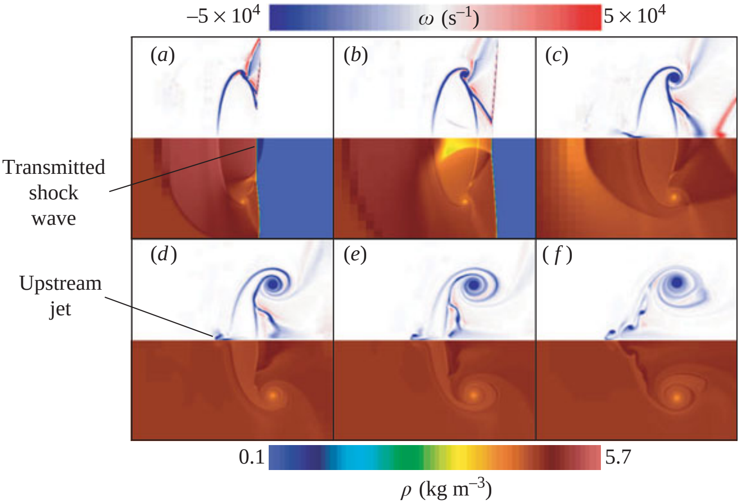

FIGURE 8. As figure 7, but for the $M=3.38$ N_2–Ar scenario ($A=0.176$): (a) $\tau=1.6$, (b) $\tau=2.6$, (c) $\tau=5.0$, (d) $\tau=10.0$, (e) $\tau=15.0$, (f) $\tau=24.9$. Note that $\tau=tW_i/R$ here.

resolved in the simulations (figure 10b), as the transmitted shock front becomes strongly concave and undergoes shock focusing. The bubble, in these cases, acts as a strongly convergent lens, refracting the shock wave toward the axis.

Diffracted shock waves become particularly important in the strongly convergent cases. Diffracted shock waves, shown schematically in figure 1(c–d), are the portions of the incident shock wave which are distorted as they sweep around the periphery of the bubble, without encountering the density interface directly. Unlike the weakly convergent nitrogen–argon scenario, in the strongly convergent cases (air–krypton and

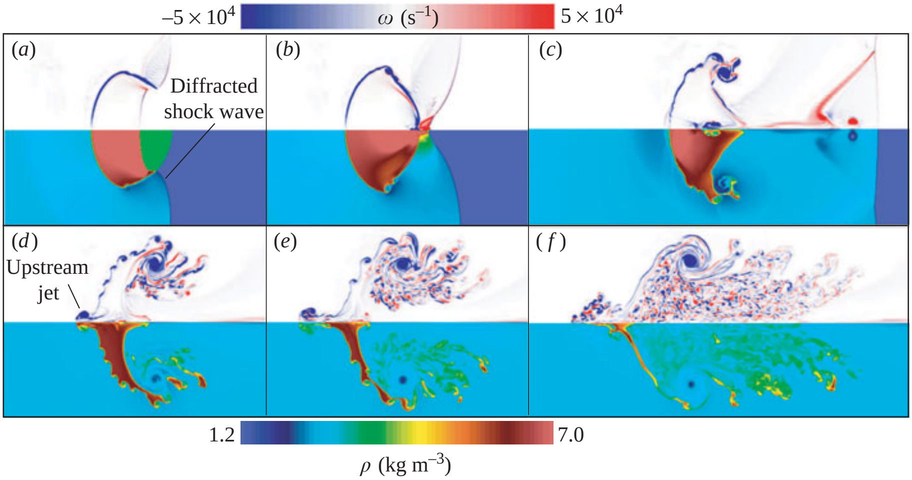

FIGURE 9. As figure 7, but for the $M=1.68$ air–Kr scenario ($A=0.486$): (*a*) $\tau=1.6$, (*b*) $\tau=2.6$, (*c*) $\tau=5.0$, (*d*) $\tau=10.2$, (*e*) $\tau=14.9$, (*f*) $\tau=25.0$. Note that $\tau=tW_i/R$ here.

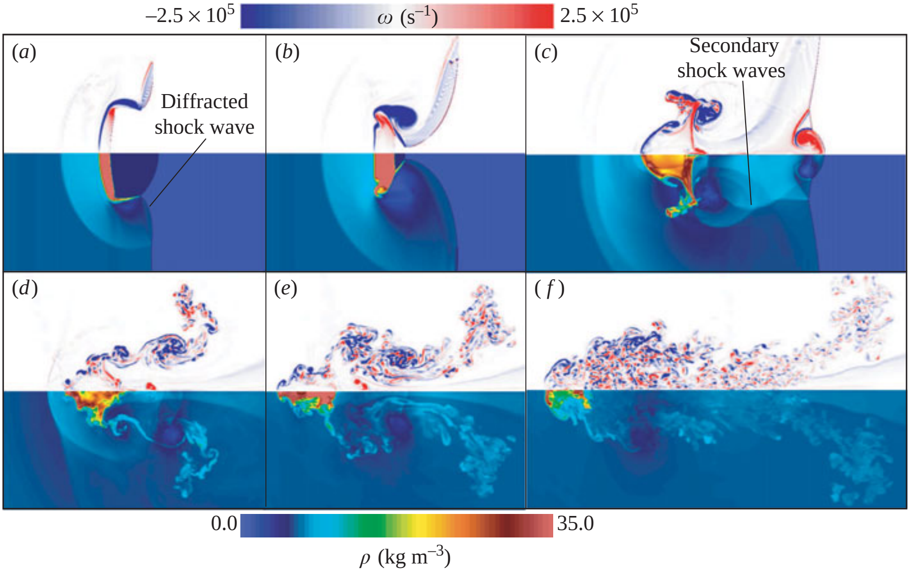

FIGURE 10. As figure 7, but for the $M=5.0$ air–R12 scenario ($A=0.613$): (*a*) $\tau=1.5$, (*b*) $\tau=2.5$, (*c*) $\tau=5.0$, (*d*) $\tau=10.1$, (*e*) $\tau=15.0$, (*f*) $\tau=25.0$. Note that $\tau=tW_i/R$ here.

air–R12), the diffracted shock wave remains nearly normal to the bubble surface at the point where it contacts the interface, while sweeping around from the equator to the downstream pole, where focusing occurs. This ‘near-normality’ behaviour, observed in simulations by Samtaney & Zabusky (1994), dramatically changes the shape of the primary shock front as it moves downstream from the vicinity of the bubble, and effectively slows the progress of vorticity deposition, as the diffracted shock wave must travel a distance equal to $(1+\pi/2)R$ to reach the downstream pole, rather than just $2R$. Thus, the diffracted shock waves do not reconverge on the downstream pole until approximately $\tau\approx2.57$, rather than 2.0, as shown in figures 9(*b*) and 10(*b*), and in the corresponding movies.

Further, because the diffracted shock waves maintain normality to the bubble surface, shock waves diffracted around opposing limbs of the bubble collide with each other when they reach the downstream pole (figure 1*d*). Shock focusing produces an intense pressure jump and initiates additional periods of baroclinic vorticity deposition as the resulting shock waves subsequently traverse the bubble in the lateral and upstream directions. Shock waves moving laterally across the bubble after such a collision are visible as curved light-blue fronts moving across a darker blue background in figure 10(*c,d*) and in the movie linked to figure 10. The effects of these secondary shocks, such as dramatic changes in the bulk density of the bubble, are known to be present as late as $\tau = 12$ (see § 6.1 and figure 18).

Another noticeable result of the intense nonlinear acoustic effects in the high-A shock–bubble interaction is the formation of a Winkler-Group vortex, as described in § 1.1, following just behind the shock wave after re-transmission into the ambient gas, seen in figures 9(*c*) and 10(*c*) (see Winkler *et al.* 1987). This opposite-signed vortex ring is also responsible for the prominent black streak seen in figure 5(*a*), running ahead of the shocked-bubble region.

In all of the heavy-bubble cases ($A > 0$), reflected and/or diffracted ('secondary') waves reverberate through the bubble after $\tau = 2$. This is due to the nature of nonlinear acoustic effects in $A > 0$ scenarios: shock waves leaving the bubble must introduce reflected rarefaction waves in the bubble gas, while, simultaneously, diffraction and focusing processes introduce secondary shock waves into the bubble region. Thus, even in the weakly convergent nitrogen–argon scenario, a rarefaction and shock wave successively pass through the bubble moving upstream after $\tau = 2$, visible as a shock-bounded yellow region in figure 8(*b*) and in the corresponding movie. These are generated by the interaction of the transmitted shock wave with the downstream interface, and by convergence of the diffracted shock waves. In the $M = 3.38$ and $M = 2.88$ scenarios, this results in a very small secondary upstream jet and vortex ring, visible at $\tau \geqslant 10$ in figure 8(*d–f*), though the effect is suppressed in the $M = 1.33$ case. This secondary upstream-directed wave may be partially responsible for secondary jets and vortices observed experimentally by Ranjan *et al.* (2005), though the effect may be magnified by the presence of soap-film material in shock-tube experiments.

It is also worth noting that inward-directed rarefactions typically do not arise in the light-bubble (convergent) cases unless the Mach number is sufficiently high; only the outward-directed spherical rarefaction wave appears, generated by the initial impact of the incident shock wave on the upstream bubble surface. Thus, the bulk density of the bubble fluid may decrease after initial shock passage in heavy-bubble (convergent) cases, but not in most light-bubble scenarios. (This is shown quantitatively in § 6.1.)

5.2. *Vorticity production and bubble deformation*

This complex field of shock waves and rarefaction waves produces an equally complex vorticity field and interface-deformation pattern in the bubble region. One of the most dramatic ways in which the bubble deforms is by the formation of prominent axial jets. An axial jet of some form arises in all of the heavy-bubble cases, except the nitrogen–argon, $M = 1.33$ case. In the other nitrogen–argon scenarios, a very weak upstream jet forms at very late times on the upstream bubble pole owing to reflections. The air–kryton and air–R12 scenarios show both upstream and downstream jetting, owing to shock focusing and strong reflections, with a particularly strong downstream jet forming in the air–R12, $M = 1.14$ case owing to shock focusing. Upstream jetting in the air–kryton, $M = 1.5$ scenario is also seen in the experiments and simulations of Layes & LeMétayer (2007). In the high-M air–krypton and air–R12 scenarios here, downstream jets are suppressed by the rapid formation of a large primary vortex ring, and upstream jetting is more prevalent, visible particularly in figure 9(*d–f*) and in the corresponding movie.

In every case in the parameter study, a distinguishable vortex ring core forms in the flow by $\tau = 15$, or much sooner in some cases. This is the expected behaviour, according to the standard description based on baroclinic vorticity deposition. In some cases, particularly nitrogen–argon, $M = 2.88$, 3.38, this vortex core is the only significant feature in the vorticity field at late times. This is true, for the nitrogen–argon cases in particular, because the relative compressibilities of the ambient and bubble gases result in a decrease of the Atwood number during shock passage. As can be seen in figure 8(*c–f*), the post-shock density contrast between bubble and ambient gases at $M = 3.38$ is very small, and this results in little additional vorticity generation after the passage of the initial shock. In most of the other scenarios, however, where the density contrast is increased by shock passage, the vorticity field continues to increase in complexity at intermediate and late times, owing to a number of effects, including the growth of Kelvin–Helmholtz instabilities on the interface and the action of the vortex-accelerated vorticity deposition mechanism described by Peng, Zabusky & Zhang (2003). Further, the intensity of the vortices can also grow, owing to the passage of secondary shock waves and rarefactions described in § 5.1. (This is examined quantitatively in § 6.3.)

In fact, in many cases, the vortical growth after initial shock passage is more dramatic and complex than the growth initiated directly by the primary incident shock wave; this is evident particularly in the movies linked to figures 9 and 10. In this sense, the shock–bubble interaction at high A is analogous to Richtmyer–Meshkov growth after reshock (see Collins & Jacobs 2002; Latini, Schilling & Don 2006), since secondary shock waves interacting with the deformed interface greatly complicate the evolution of the interface and the vorticity field.

In the high-Mach-number air–R12 cases, the vorticity field becomes so complex that the primary vortex core becomes almost indistinguishable at late times, owing to the combined intensity of the effects described above (see figure 10*f*), and owing to the azimuthal transport of vorticity. The vigorous secondary vorticity generation and transport eventually leads to the development of an amorphous distribution of intense and disorderly vortical perturbations, with characteristics that we speculate might be best described loosely as ‘chaotic’ or ‘turbulent’. Associated with the intense field of vortical fluctuations and disorderly motion is a region of intense mixing. The shocked bubble is effectively reduced to a small core of compressed fluid, trailing behind a complex plume-like structure exhibiting well-developed mixing. These results indicate a much more amorphous and chaotic flow field at late times than is seen in the results from two-dimensional simulations shown in figure 14 of ZZ, or in the results for the $M = 2.5$ two-dimensional test problem shown here in figure 4. The two-dimensional simulations show a late-time flow field dominated by large distinct vortex rings and vortex projectiles, while the three-dimensional simulations capture the complex and often disordered morphology of a turbulent flow field resulting from the transport of mass, momentum and energy in all three spatial dimensions.

6. Integral diagnostics

In order to evaluate the performance of several types of analytical models and scaling laws across the parameter space of the present study, and to deepen the understanding of the phenomena described above, four integral diagnostics are applied to the data generated in these 14 scenarios. These include diagnostics for the total volumetric bubble compression, the mean bubble streamwise velocity, the velocity circulation and its positive and negative components, and the extent of mixing.

6.1. *Bulk volumetric compression*

The response of the bubble to the compressive effects of interaction with the initial shock wave and the subsequent scattered shock and rarefaction waves is characterized by tracking the mean density of the bubble fluid. Giordano & Burtschell (2006) have proposed a simple model based completely on one-dimensional gasdynamics, which, in many cases, can predict the final mean density of the bubble fluid at late times after shock passage, with good accuracy. In their model, the passage of a shock wave across the bubble is modelled using the known evolution of gas properties during the passage of a shock wave across a discrete slab inhomogeneity in a gas medium. At each encounter between the shock wave and an interface, properties of the resulting transmitted and reflected waves are computed from the initial conditions by iteratively solving a system of equations derived from one-dimensional gasdynamics. By tracking the density changes in the slab through the passage of a sufficient number of these transmitted and reflected waves, we arrive at a 'final' bulk density for the slab. Such a methodology can be appropriate only until a rarefaction wave has passed through the slab, at which point the dimension of the slab and the thickness of the rarefaction wave dictate subsequent behaviour. In the heavy-bubble configuration, a reflected rarefaction wave is produced when the shock interacts with the downstream interface, and, consequently, only the first two shock reflection/transmission events may be tracked. However, in the light-bubble configuration, only shock waves are reflected back into the slab, and any desired number of events may be tracked.

In this one-dimensional model, a final density ρ_2'' is computed after the transit of two waves: (i) the initial transmitted shock wave and (ii) the internally reflected shock wave or rarefaction wave. Giordano & Burtschell (2006) have compared experimental and computational results to this model by regarding ρ_2'' as the final average density of bubble fluid and invoking conservation of mass, so that $\mathscr{V}_f/\mathscr{V}_0=\rho_2/\rho_2''$, where ρ_2 is the (unshocked) density at which the bubble fluid is initialized, $\mathscr{V}_f$ is the final or asymptotic bubble fluid volume, and $\mathscr{V}_0$ is the initial unshocked bubble volume. The resulting ratios of final to initial volume $\mathscr{V}_f/\mathscr{V}_0$ were then compared to volume ratios obtained from both two-dimensional axisymmetric simulations and shock-tube experiments, for one air–helium case and one air–krypton case. The volume they measured from simulations is a 'species volume', or a weighted sum of partial volumes in each cell, written in integral form as

$$\mathscr{V}^*(t)=\int_D f(x,y,z,t)\,\mathrm{d}\mathscr{V}, \tag{6.1}$$

where $\mathscr{V}^*(t)$ is the total weighted volume of the bubble fluid, $f(x,y,z,t)$ is the local volume fraction of bubble fluid, and D is the entire computational domain. By measuring the weighted volume rather than the total volume of the $f>0$ region, the effects of compressibility are not conflated with the effects of mixing. The computational results shown by Giordano & Burtschell (2006) indicate that the total weighted volume is abruptly driven downward during initial shock passage, then, for heavy-bubble cases, oscillates briefly as secondary reflected and diffracted shock waves pass over the bubble and, finally, approaches an asymptotic value near to that predicted by the one-dimensional model.

In order to compare our computational results to the one-dimensional model, measured values of $\mathscr{V}^*(t)$ from simulations (obtained by evaluating the integral in (6.1)) are first recast as measured values of the 'compression ratio' C, using $C(t)\equiv\mathscr{V}_0/\mathscr{V}^*(t)$. For ease of comparison among scenarios with differing M and A,

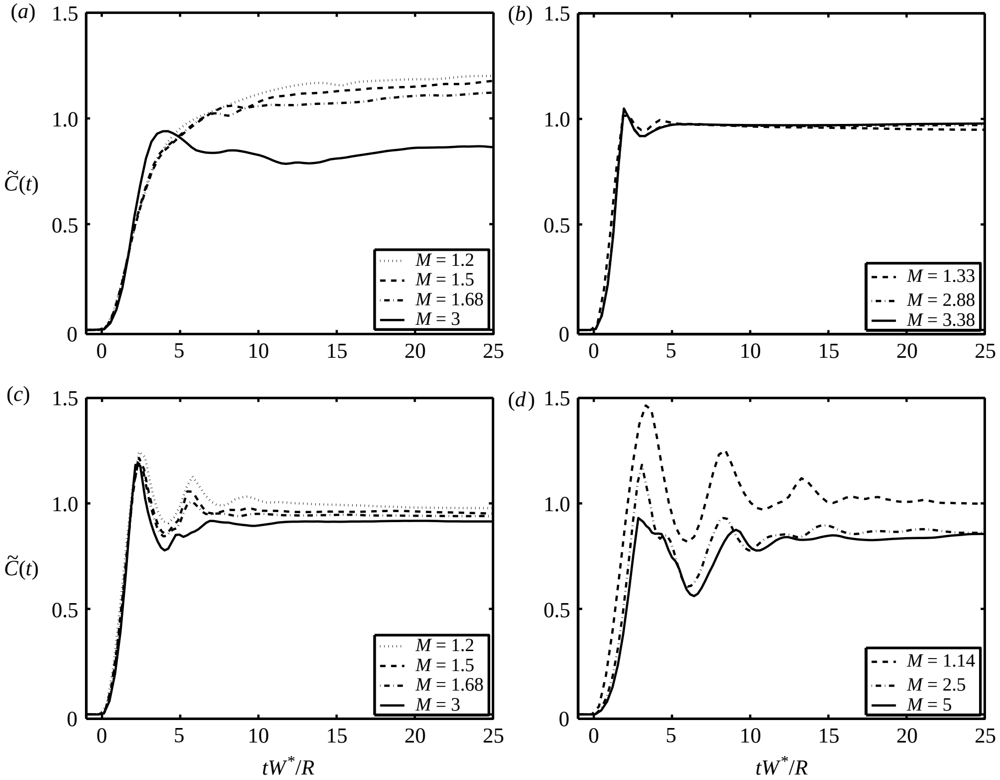

FIGURE 11. Plots over dimensionless time of the shocked-bubble compression factor obtained from three-dimensional simulations, normalized to the compression factor obtained from the one-dimensional gasdynamics model of Giordano & Burtschell (2006), using (6.2): (*a*) air–He, $A = -0.757$; (*b*) N_2–Ar, $A = 0.176$; (*c*) air–Kr, $A = 0.486$; and (*d*) air–R12, $A = 0.613$.

the values $C(t)$ are then normalized to the one-dimensional model as

$$\tilde{C}(t) = \frac{C(t) - 1}{C_2'' - 1}, \tag{6.2}$$

where

$$C_2'' = \frac{\mathscr{V}_0}{\mathscr{V}_f^{1D}} = \frac{\rho_2''}{\rho_2}. \tag{6.3}$$

Under this normalization, $\tilde{C}(0) = 0$ by definition, and $\tilde{C} = 1$ represents the one-dimensional-gasdynamics limit. Thus, for a successful model prediction, $\tilde{C}(t) \rightarrow 1$ as $t \rightarrow \infty$. The normalized compression ratio can be expressed in terms of densities as

$$\tilde{C}(t) = \frac{\langle \rho(t) \rangle - \rho_2}{\rho_2'' - \rho_2}, \tag{6.4}$$

where $\langle \rho(t) \rangle$ represents the volume-averaged partial density of bubble fluid.

The time-dependent compression ratio for bubble fluid, $\tilde{C}(t)$, is plotted with this one-dimensional-gasdynamics normalization on the dimensionless time scale tW^*/R for all 14 scenarios in figure 11. In these plots, the compression history of the shocked bubble collapses nearly to a single trend within each gas pairing, except for the unusual behaviour in the air–helium, $M = 3$ scenario. For the heavy-bubble scenarios (figure 11*b–d*), the compression ratio of the bubble fluid oscillates about the one-dimensional-gasdynamics limit for a short time after initial shock passage, as secondary shock waves and rarefaction waves reverberate through the bubble region. The compression ratio initially increases owing to the transit of the primary shock wave, then decreases as a reflected expansion wave moves across the bubble, then increases owing to shock focusing. Oscillations continue as shock waves introduce compression phases, and rarefaction waves introduce decompression phases.

The strength and duration of these oscillations in the heavy-bubble scenarios increase more strongly with A than with M. This is because the strength of secondary shock waves and the complexity of the refraction pattern drastically increase as the refractive power of the bubble increases. As the intensity of secondary shock waves grows, the length of time t_s during which $\tilde{C}$ continues to oscillate about unity also increases. For the nitrogen–argon cases, this time is only roughly $t_s = 5R/W^*$, whereas in the air–krypton and air–R12 cases, it increases to $11R/W^*$ and $15R/W^*$, respectively.

No such oscillations are apparent in the light-bubble scenarios, for $M < 3$ (figure 11*a*). In these scenarios, the compression factor for bubble gas increases nearly monotonically. This is a manifestation of the absence of rarefaction waves from the bubble gas during the transit of primary and secondary waves. In the light-bubble cases, all internally reflected waves are shock waves, and no decompression phases are observed in the compression trends. This is not the case in the $M = 3$ scenario, however. The compression factor suddenly drops shortly after the initial transient. This indicates that at high Mach number, intensified nonlinear-acoustic effects give rise to waves in the air–helium scenarios that are not present for $M < 2$, which allow the bubble gas to expand. This also suggests that the upstream, trailing helium lobes or 'rings' which persist to late time for $M < 1.3$ (see Layes *et al.* 2005), but are diminished dramatically for $M \approx 3$ (see Ranjan *et al.* 2007), play a significant role in the coupling of the bubble gas bulk compression to the transit of the primary shock wave and the field of secondary waves.

The collapse of these data to a nearly self-similar trend is particularly remarkable in the nitrogen–argon and air–krypton cases (figure 11*b, c*). For these scenarios, the Giordano–Burtschell model prediction is accurate to within less than 7% for late times ($tW^*/R > 10$), across a very broad interval in M. The bubble mean density thus appears to equilibrate to a value near that predicted by the one-dimensional theory, suggesting that refractive effects are significant only during the initial transient phase for these cases. For the two gas pairs with highest magnitude of A, however, i.e. air–helium and air–R12 (figure 11*a, d*), the model is less accurate, and its accuracy deteriorates with increased Mach number.

Although the time scale shown here is based on W^*, a number of other time scales were tested, but none showed the collapse seen in figure 11, where oscillations in $\tilde{C}$ for $A > 0$ are in phase within each gas pairing. However, it is clear that with this time scaling, oscillations in $\tilde{C}$ have differing periods at different Atwood numbers, since secondary shock waves acting on the bubble fluid density have speeds that depend not only on M but also on A. This dependence is highly nonlinear, since a small change in A can introduce a significant change in the shock refraction, reflection and diffraction pattern. The problem thus has a fundamentally different character at each value of A. For fixed A, however, figure 11 shows that the time scales for bubble fluid compression are set by shock-wave speeds, and the Mach number can thus be scaled out, particularly for the initial transient phase.

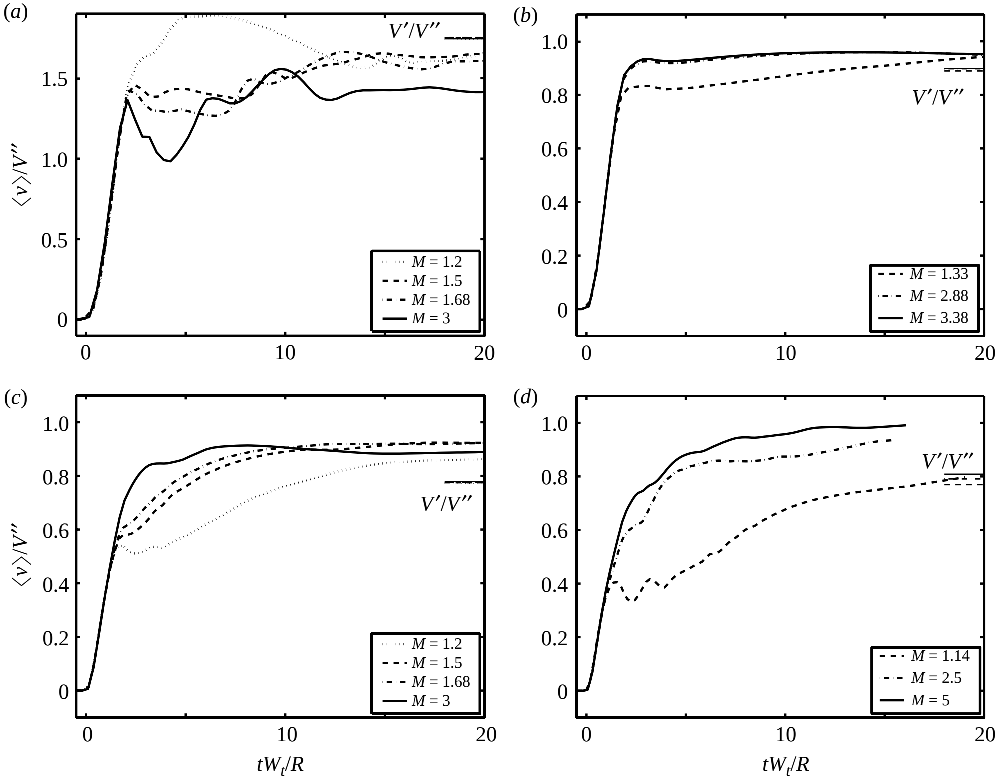

FIGURE 12. Plots over dimensionless time of the shocked-bubble mean velocity $\langle v \rangle$ obtained from three-dimensional simulations. Velocities are normalized to the y-velocity V'' obtained from a one-dimensional gasdynamics analysis similar to that of Giordano & Burtschell (2006): (*a*) air–He, $A = -0.757$; (*b*) N_2–Ar, $A = 0.176$; (*c*) air–Kr, $A = 0.486$; and (*d*) air–R12, $A = 0.613$. Line segments at the right-hand margin indicate the ratio V'/V''.

6.2. *Mean bubble fluid velocity*

The approach of Giordano & Burtschell (2006), based on one-dimensional gasdynamics, can also be used to predict other integral properties of the bubble gas after the transit of the primary shock wave and the series of secondary waves. The same analysis can be used to obtain, first, the streamwise velocity V' in the slab inhomogeneity after the passage of the initial transmitted shock and, secondly, the streamwise velocity V'' in the inhomogeneity after the passage of the internally reflected wave. Comparison of these modelled velocities to the volume-averaged bubble y-velocity $\langle v(t) \rangle$ obtained from the present simulations shows that the bubble velocity at late time is bounded by V' and V''.

The mean bubble y-velocity is computed from simulations as

$$\langle v(t) \rangle = \frac{3}{\pi R^3 \rho_2} \int_D \rho_b f v \, \mathrm{d}\mathscr{V}, \tag{6.5}$$

where ρ_b is the local partial density of bubble fluid, f is the bubble fluid volume fraction, v is the local y-velocity and $\pi R^3 \rho_2 / 3$ is the total mass of the quarter-spherical bubble. Mean bubble velocities obtained using (6.5) are normalized as $\langle v(t) \rangle / V''$ and plotted on a dimensionless time scale for each scenario in figure 12. Also indicated on each plot at the right-hand margin is the ratio V'/V'', which varies only slightly with

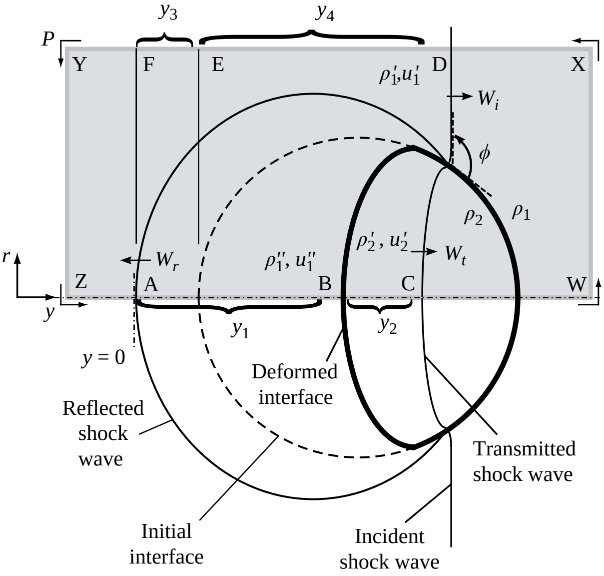

FIGURE 13. Schematic diagram of the heavy-bubble shock–bubble interaction for $t < 2R/W_t$, showing notation used in computing and modelling the circulation in the flow. Incident shock wave propagation is left-to-right.

M for fixed A. Note that for light-bubble scenarios, $V'' < V'$, because the internally reflected wave is a shock wave; however, for heavy-bubble scenarios, the internal reflection is an rarefaction wave, so $V'' > V'$.

The dimensionless time scale chosen for the plots of the mean bubble velocity in figure 12 is tW_t/R. The time scale is thus based on the transmitted wave speed, rather than W_i or W^*; this time scale yields the best collapse of the velocity data during the initial transient ($tW_t/R < 2$). This confirms that time scales for bubble fluid acceleration during shock transit are set by the transmitted shock-wave speed. At late times, the bubble fluid mean velocity equilibrates to a value bounded by V' and V''. In all heavy-bubble scenarios, we observe that $V'/V'' < \langle v(t) \rangle < 1$ for $t \to \infty$. In the light-bubble cases, $1 < \langle v(t) \rangle < V'/V''$ for $t \to \infty$. Thus, the one-dimensional analysis yields a useful tool for predicting the final bubble fluid velocity.

6.3. *Circulation*

Another method by which the shock–bubble interaction has commonly been understood and modelled is by means of measuring the circulation – that is, the circulation of the velocity field about a path P enclosing a diametral half-plane in the flow field. One leg of P lies on the axis of symmetry (the y-axis, here), and the opposite leg lies on a parallel line outside the region of non-zero vorticity, as shown in figure 13.

For the path P, the circulation is defined as

$$\Gamma = \oint_P \boldsymbol{V} \cdot \mathrm{d}\boldsymbol{s}, \tag{6.6}$$

which, by Stokes' theorem, is equivalent to the area integral of vorticity:

$$\Gamma = \int_S \boldsymbol{\omega} \cdot \mathrm{d}A, \tag{6.7}$$

where S is the area bounded by P. Thus, the circulation, here, quantifies the net strength of the vortex rings generated by the shock-bubble interaction. For this reason, it has been the subject of a number of analytical models with various conceptual bases. Four models are considered here and compared to the results of the present calculations, including the formulations of Picone & Boris (1988) (hereinafter referred to as PB), Yang *et al.* (1994) (hereinafter, YKZ), Samtaney & Zabusky (1994) (hereinafter, SZ) and a new model proposed as part of the present study.

Each of these models predicts the total circulation present in the flow at the instant of shock passage. This is the moment at which the fastest shock wave in the system reaches the downstream pole of the bubble and reflected waves are generated. For the air–helium scenarios, this instant corresponds to $tW_t/R = 2.0$. For the nitrogen–argon cases, it is given by $tW_i/R = 2.0$. However, in the air–krypton and air–R12 cases, the instant of first shock passage is delayed owing to the curvature of the diffracted shock. That is, because of the large refractive power of the bubble (large A) in these cases, the portion of the shock front in contact with the bubble surface remains normal to the interface after it has moved downstream of the bubble equator. Defining ϕ to be the angle between the plane of the unperturbed shock front and the tangent plane to the bubble surface at the point of contact with the shock wave, the shock wave must traverse a distance $\pi R/2$ for $\phi \geqslant \pi/2$, rather than merely R, before reaching the downstream ($\phi = \pi$) surface of the bubble. Thus, the progress of the shock wave across a distance $2R$ is effectively slowed by a factor of $2/(1+\pi/2)$ in these scenarios, as discussed in § 5.1. Therefore, we construct an 'effective' shock wave speed $\tilde{W}$ for time scaling, to account for this effect:

$$\tilde{W} = \begin{cases} W_t, & A < 0, \\ W_i, & 0 \leqslant A \leqslant 0.2, \\ 2W_i/(1+\pi/2), & A > 0.2. \end{cases} \tag{6.8}$$

The circulation at the instant of first shock passage is then defined as

$$\hat{\Gamma} = \Gamma|_{t=2R/\tilde{W}}, \tag{6.9}$$

and corresponds to the circulation at the 'end of phase (iii)', in the terminology of Samtaney & Zabusky (1994). Only a time scale based on $\tilde{W}$ will place the shock-passage circulation at the same dimensionless time for every scenario.

6.3.1. *Circulation models based on integrated baroclinic torque*

To obtain the total circulation at shock passage, in the models of PB and YKZ, the baroclinic source term in the vorticity equation is integrated over the half-plane and over the time during which the shock wave initially passes over the bubble, with some simplifying assumptions. The two models assume that both the shape of the bubble and the density ratio relative to its surroundings do not change significantly during initial shock passage, and that the shock front proceeds in linear fashion across the bubble with no changes in its shape or speed. Vorticity production is then decoupled from shock refraction and diffraction, so that the density gradient and pressure gradient components of the baroclinic source term can be evaluated using parameters from the one-dimensional shocked gas slab analogue, such as the incident shock wave speed W_i, the shocked ambient flow speed u'_1 and the density of the shocked ambient gas ρ'_1. Of the scenarios included in the current study, only in the nitrogen–argon $M = 1.33$ case are these criteria nearly met. However, the formulae can be regarded as first-order estimates of the circulation resulting from only the passage of the initial shock wave, neglecting the higher-order effects associated with shock refraction, focusing, diffraction and reflections. The PB model (see Picone *et al.* 1985; Picone & Boris 1988), in our notation, is given by

$$\Gamma_{\mathrm{PB}} = 2u_1'\left(1 - \frac{u_1'}{2W_i}\right) R \ln\left(\frac{\rho_1}{\rho_2}\right), \tag{6.10}$$

and the YKZ model by

$$\Gamma_{\mathrm{YKZ}} = \frac{4R}{W_i}\frac{p_1' - p_1}{\rho_1'}\left(\frac{\rho_2 - \rho_1}{\rho_2 + \rho_1}\right). \tag{6.11}$$

6.3.2. *Circulation model motivated by asymptotics*

An entirely different approach is taken in the SZ model (see Samtaney & Zabusky 1994; Samtaney, Ray & Zabusky 1998; Zabusky & Zeng 1998), which captures shock refraction effects by invoking scaling arguments derived from shock polar analysis (see Henderson 1966, 1989) and from numerical simulations of shock-wave interactions with planar interfaces across a broad parameter space. An 'asymptotically motivated' analysis in Samtaney & Zabusky (1994) yields a general first-order-accurate scaling law for the rate of circulation deposition per unit unshocked interface length, for an interface of arbitrary shape. For the fast/slow configuration and unit ambient unshocked density and pressure (and thus sound speed $\gamma^{1/2}$), their formulation is given as

$$\frac{\mathrm{d}\Gamma_1}{\mathrm{d}s} = \frac{2\gamma^{1/2}}{\gamma + 1}\left(1 - \chi^{-1/2}\right)\sin\phi\left(1 + M^{-1} + 2M^{-2}\right)(M - 1), \tag{6.12}$$

where s is a path length along the interface, $\chi = \rho_2/\rho_1$, ϕ is the local inclination of the unshocked interface relative to the unperturbed incident shock front (labelled in figure 13) and γ is a characteristic ratio of specific heats for the flow, e.g. $\gamma = (\gamma_2 + \gamma_1)/2$.

This formula is an approximation to the exact expression for the circulation associated with regular refraction of a shock wave at a planar interface, given by Samtaney & Zabusky (1994) (SZ) as equation (2.11). The scaling law (6.12) possesses a number of desirable properties. First, the $\sin\phi$ factor ensures that $\mathrm{d}\Gamma/\mathrm{d}s$ has the same sign and periodicity as $\nabla\rho \times \nabla p$. Also, the circulation deposition scales linearly with M for large M, asymptotes to zero for $M \rightarrow 1$ and is independent of χ for large χ. This formula has been used, with success, to predict the circulation on sinusoidal, circular and elliptical interfaces accelerated by shock waves of various strengths (see Samtaney & Zabusky 1994; Zabusky & Zeng 1998; Zabusky 1999; Ray, Samtaney & Zabusky 2000).

The use of this scaling law here, however, is presented with two qualifiers. First, in this form, it is only applicable for fast/slow refraction scenarios, and thus can only be applied to heavy-bubble shock–bubble interactions in the present study. An extension of the theory to the slow/fast configuration, for shocked planar inclined gas interfaces, has been derived and validated using Eulerian simulations by Samtaney *et al.* (1998). (Values computed using this extension, adapted for circular interfaces, are shown here in table 3.) Secondly, for planar inclined gas interfaces, SZ have computed the circulation using both the exact expression and the scaling law shown here (6.12), for a series of inclination angles ϕ, Mach numbers M and density ratios χ (plotted in figure 15 of SZ). SZ regard the scaling law as valid only in the parameter space subregion where the difference between the two is less than 10%, and shock refraction does not become irregular. Since most of the scenarios considered here fall

Scenario number	Gases	M	$\hat{\varGamma}_0$ (m^2 s^{-1})	$\varGamma_{PB}$ (m^2 s^{-1})	$\varGamma_{YKZ}$ (m^2 s^{-1})	$\varGamma_{SZ}$ (m^2 s^{-1})	$\varGamma_{SZ3}$ (m^2 s^{-1})	$\varGamma_{1D}$ (m^2 s^{-1})
1	Air–He	1.20	4.98	9.20	5.98	21.05	−6.93	5.47
2		1.50	10.09	18.41	9.84	31.25	11.42	11.53
3		1.68	12.50	22.79	11.04	34.93	24.04	14.50
4		3.00	24.93	48.26	15.25	44.85	77.89	31.24
5	N_2–Ar	1.33	−1.95	−2.48	−1.91	−2.16	−1.99	−1.98
6		2.88	−4.25	−8.41	−3.50	−6.79	−5.09	−3.88
7		3.38	−4.68	−10.01	−3.82	−7.96	−5.23	−4.29
8	Air–Kr	1.20	−4.38	−4.93	−3.84	−4.69	−4.08	−5.85
9		1.50	−8.56	−9.88	−6.32	−9.30	−9.12	−9.63
10		1.68	−10.39	−12.23	−7.09	−11.40	−11.45	−11.05
11		3.00	−18.16	−25.90	−9.79	−22.64	−22.19	−18.74
12	Air–R12	1.14	−3.89	−4.93	−3.82	−4.82	−4.05	−5.33
13		2.50	−22.06	−28.32	−11.22	−25.97	−25.43	−21.89
14		5.00	−43.28	−59.75	−17.10	−51.55	−48.95	−43.73

TABLE 3. Computed and modelled values of primary circulation at the instant of first shock passage ($t\tilde{W}/R = 2$) for each of the 14 scenarios and each of the models described in §§ 6.3.1–6.3.3.

in the region of irregular refraction even at $\phi = \pi/3$, we proceed with the scaling-law formulation (6.12) only as a means of estimating the circulation.

To obtain the circulation in the shocked bubble, SZ integrate (6.12) along a half-circumference of the bubble (from $\phi = 0$ to $\phi = \pi$). (The result is identical for both spherical and cylindrical bubbles.) The formula is modified for $\phi > \pi/2$ to account for diffraction of the shock wave propagating around the bubble interface, by invoking a 'near-normality' hypothesis. This takes into account the empirical observation that the diffracted shock wave maintains its front at 90° to the unshocked bubble surface, in the case of $A > 0.2$ where shock-wave curvature is significant. Thus, the substitution $\sin\phi = 1$ is made in the second half of the integral, for $\pi/2 < \phi \leqslant \pi$. In the case of $0 < A < 0.2$, we observe that the near-normality hypothesis does not hold, and this substitution is therefore not made. This yields the following formula for the circulation:

$$\varGamma_{SZ} = \begin{cases} \left(\dfrac{4}{1+\gamma}\right)\left(1-\chi^{-1/2}\right)\left(1+M^{-1}+2M^{-2}\right)(M-1)\,Rc_1, & 0 < A < 0.2, \\ \left(1+\dfrac{\pi}{2}\right)\left(\dfrac{2}{1+\gamma}\right)\left(1-\chi^{-1/2}\right)\left(1+M^{-1}+2M^{-2}\right)(M-1)\,Rc_1, & A \geqslant 0.2, \end{cases} \tag{6.13}$$

where the dimensionless scaling law (equation (5.15) of SZ) has been multiplied by the ratio $c_1/\gamma^{1/2}$, in order to obtain the circulation in physical units. Zabusky & Zeng (1998) have used this formula (for $A > 0.2$) to predict the circulation present in the shocked bubble flow, simulated using a two-dimensional Godunov code, just after passage of the initial shock wave, for the air–R12 scenario at $M = 1.14$, 1.5, 2.5, 5.0. It should be noted, however, that the formula appearing in ZZ as equation (26) contains a unnecessary additional factor of $\gamma^{1/2}$, and the intended form is that shown here in (6.13).

The scaling law (6.12), which is the basis of this formula, is derived by SZ as a first-order approximation to the circulation per unit length. A third-order-accurate correction to (6.12) is proposed in Appendix A.2 of SZ. After integrating around the bubble and incorporating this third-order extension in the scaling law (following equation (5.11) of SZ), a third-order-accurate version of the SZ model (hereinafter, 'SZ3') is then written as

$$\Gamma_{SZ3} = \Gamma_{SZ} + \frac{1}{\gamma^{1/2}}\left(\frac{2}{3} + \frac{\pi}{2}\right)\Gamma_3' R c_1, \tag{6.14}$$

where the form of Γ_3' is given in Appendix A.2 of SZ. The inclusion of the third-order-accurate extension introduces a change of more than 10% only in the nitrogen–argon, $M = 2.88, 3.38$ and air–krypton, $M = 1.2$ cases, but the results presented in §6.3.4 generally show better accuracy with respect to computed values when this third-order correction is included. The values computed using the first-order- and third-order-accurate formulations are shown here in table 3.

6.3.3. *Circulation model based on one-dimensional gasdynamics*

We propose a third approach to modelling the circulation, in which the velocity field at shock passage is reconstructed using one-dimensional gasdynamics parameters and fits to computational data across the parameter space. The circulation is computed using line integrals over this reconstructed field. Consider the velocity field $\boldsymbol{V}$ at the instant of shock passage. The circulation associated with this field can be obtained by integrating the velocity along a path P identical to that shown enclosing the grey area in figure 13, except that at shock passage, the points C and D on the path are advanced downstream to locations near the line $y = 2R$. Using this path of integration, the circulation can be computed exactly as

$$\Gamma = \int_{\mathrm{A}}^{\mathrm{B}} \boldsymbol{V}\cdot\hat{y}\,\mathrm{d}y + \int_{\mathrm{B}}^{\mathrm{C}} \boldsymbol{V}\cdot\hat{y}\,\mathrm{d}y + \int_{\mathrm{D}}^{\mathrm{E}} \boldsymbol{V}\cdot\hat{y}\,\mathrm{d}y + \int_{\mathrm{E}}^{\mathrm{F}} \boldsymbol{V}\cdot\hat{y}\,\mathrm{d}y, \tag{6.15}$$

where it is noted that there is no contribution to the integral along the path P from the line segments $\overline{\mathrm{CW}}$, $\overline{\mathrm{WX}}$, $\overline{\mathrm{XD}}$ and $\overline{\mathrm{YZ}}$; and that the contributions from the line segments $\overline{\mathrm{FY}}$ and $\overline{\mathrm{ZA}}$ cancel. Let the path of integration be arranged such that the line segment $\overline{\mathrm{DF}}$ lies in a region where $\boldsymbol{V} = u_1'\hat{y}$, and the line segment $\overline{\mathrm{AC}}$ lies on the axis of symmetry, where $\boldsymbol{V}\cdot\hat{r} = 0$. Then the expression in (6.15) becomes

$$\Gamma = \int_{\mathrm{A}}^{\mathrm{B}} v_{\mathrm{AB}}(y)\,\mathrm{d}y + \int_{\mathrm{B}}^{\mathrm{C}} v_{\mathrm{BC}}(y)\,\mathrm{d}y - u_1'(y_3 + y_4), \tag{6.16}$$

where the axial velocities $v_{\mathrm{AB}}(y)$ and $v_{\mathrm{BC}}(y)$ and the distances y_3 and y_4 must be modelled. By solving the one-dimensional gasdynamics equations iteratively for the transmission of a normal shock wave into a slab of gas whose properties are known, we may obtain the reflected shock wave strength M_r and speed W_r, the speed of the transmitted shock wave W_t and the particle speed behind the transmitted shock wave u_2'. Two-dimensional simulations within the present parameter space suggest, further, that the on-axis gas velocity in the region between the interface ($y = y_1$) and the spherical reflected shock wave ($y = 0$) may be modelled as

$$v_{\mathrm{AB}}(y) = -u_1' + (u_1' - u_2')\left(\frac{y}{R}\right)^2, \tag{6.17}$$

where the coordinate system in figure 13 has been chosen such that the origin is fixed to the on-axis location of the reflected shock wave, and u_2' is the post-shock velocity in fluid 2. The y^2 term ensures that the reconstructed velocity behind the reflected shock wave varies nonlinearly in y as we would expect for a spherical expanding wave; this formulation has been obtained by fits to two-dimensional simulation results.

If we also substitute u_2' for v_{BC} in (6.16) (i.e. neglect the on-axis effects of shock refraction and focusing), and evaluate the remaining line integrals, we obtain an estimate of the circulation based on the one-dimensional gasdynamics reconstruction,

$$\Gamma_{\mathrm{R}} = u_1' y_1 + \tfrac{1}{3} R(u_1' - u_2') \left(\frac{-y_1}{R}\right)^3 + u_2' y_2 - u_1'(W_i t^* + y_3), \tag{6.18}$$

where the lengths of the line segments y_1, y_2, y_3 and y_4 are also obtained from one-dimensional gasdynamics as

$$\left.\begin{aligned} & y_1 = \frac{1}{\sqrt{M_r}} \left(u_2' + W_r\right) t^*, \quad y_2 = (W_t - u_2') t^*, \quad y_3 = \frac{W_r t^*}{\sqrt{M_r}}, \quad y_4 = W_i t^*, \\ & t^* = \frac{2R}{\tilde{W}}. \end{aligned}\right\} \tag{6.19}$$

All velocity quantities are obtained from one-dimensional gasdynamics, and the segment length reduction factor $1/\sqrt{M_r}$ appearing in (6.19) is a scaling factor which accounts for the curvature and time-dependent weakening of the reflected spherical shock wave. It is determined empirically from numerical simulations for the shock–bubble interaction in a method similar to that by which scaling factors in the model of Samtaney & Zabusky (1994) were obtained. Although the four terms appearing in (6.18) all have the same order of magnitude and partially offset each other for the present scenarios, the fourth term – associated with the on-axis velocity induced by the incident shock wave – is the dominant term in nearly all of the simulations shown here. Further, we note that although $\Gamma_R \to 0$ for $M \to 1$, the model has no asymptote for $M \to \infty$. In this sense, the model should only be regarded as a useful estimate for the circulation with the parameter space of the present study, since it cannot be shown to have consistent asymptotic behaviour in the same sense as the SZ model.

6.3.4. *Circulation obtained from simulations*

To compare the results of the current simulations with these models, a procedure is defined for measuring the velocity circulation from three-dimensional data. The circulation is measured as a function of the azimuthal coordinate θ, using a series of 48 sample planes at incremented azimuthal θ-locations,

$$\theta_k = \frac{k-1}{47}\frac{\pi}{2}, \quad k = 1, \ldots, 48. \tag{6.20}$$

For each of the 48 azimuthal locations, a planar slice is taken through the dataset, defined by normal vector $\hat{n}_k = \hat{\theta}_k = (\cos(\theta_k), 0, -\sin(\theta_k))$ and anchored at the origin. The circulation is computed by evaluating the integral in (6.7) over this slice to obtain the net circulation $\Gamma_0(\theta_k, t)$. The positive component of the circulation $\Gamma_+(\theta_k, t)$ and negative component of circulation $\Gamma_-(\theta_k, t)$ are obtained by only including $\omega > 0$ and $\omega < 0$, respectively, in the integral. For the heavy-bubble scenarios included in this study, vorticity deposition by the initial shock wave produces 'negative' rotation in the sense that $\omega = \boldsymbol{\omega} \cdot \hat{\theta} < 0$, and in the air–helium cases, 'positive' rotation ($\boldsymbol{\omega} \cdot \hat{\theta} > 0$) is produced by the initial shock wave. This we call 'primary' circulation, corresponding to $\Gamma_-(\theta, t)$ for the heavy-bubble scenarios (nitrogen–argon, air–krypton and air–R12), and $\Gamma_+(\theta, t)$ for the light-bubble scenarios (air–helium).

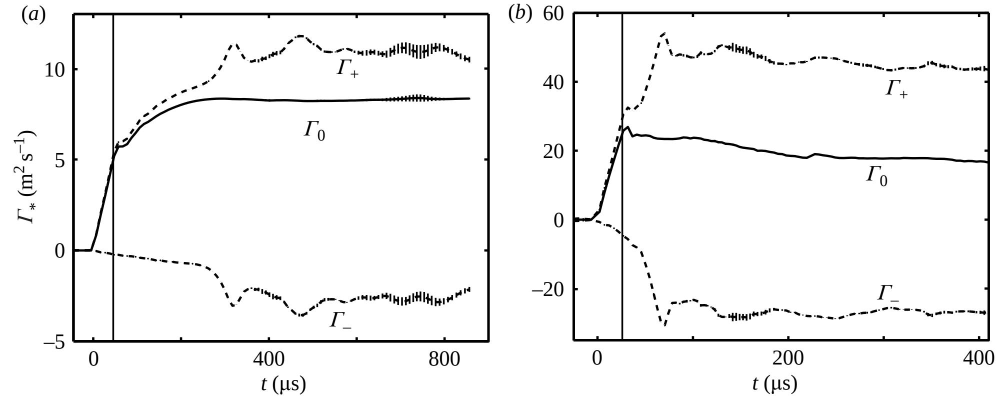

FIGURE 14. Decomposed circulation Γ_* versus time, for two air–He scenarios: (*a*) $M = 1.2$, and (*b*) $M = 3.0$. Vertical bars indicate r.m.s. azimuthal fluctuations $\tilde{\Gamma}_*$ and a solid vertical line indicates the time of shock passage, $t^* = 2R/\tilde{W}$.

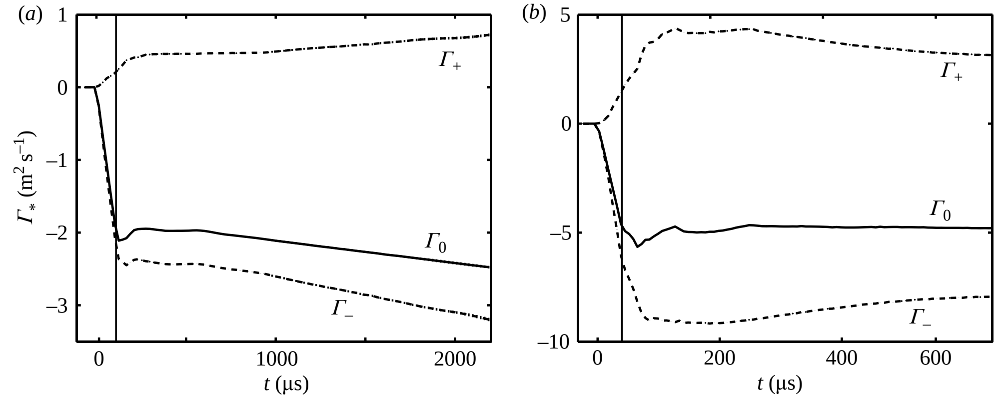

FIGURE 15. As for figure 14, but for two N_2–Ar scenarios: (*a*) $M = 1.33$, and (*b*) $M = 3.38$.

Azimuthally averaged values of the positive, negative and net circulation in the bubble region are obtained as

$$\bar{\Gamma}_*(t) = \frac{2}{\pi}\int_0^{\pi/2} \Gamma_*(\theta, t)\,\mathrm{d}\theta \approx \frac{1}{48}\sum_{k=1}^{48} \Gamma_*(\theta_k, t), \tag{6.21}$$

where $* \in \{+, -, 0\}$. Further, root mean square (r.m.s.) fluctuations $\tilde{\Gamma}_*(t)$ with respect to the azimuthal mean are computed by taking the variance of the 48 θ-samples:

$$\tilde{\Gamma}_*(t) = \frac{2}{\pi}\sqrt{\int_0^{\pi/2} [\Gamma_*(\theta, t) - \bar{\Gamma}_*(t)]^2\,\mathrm{d}\theta} \approx \frac{1}{48}\sqrt{\sum_{k=1}^{48} [\Gamma_*(\theta_k, t) - \Gamma_*(t)]^2}. \tag{6.22}$$

Plots of $\bar{\Gamma}_*(t)$ are given in figures 14 to 17 for the highest- and lowest-Mach-number scenarios for each gas pairing included in this study. The time of shock passage, $t^* \equiv 2R/\tilde{W}$ is indicated on each plot by a solid vertical line. The r.m.s. azimuthal fluctuations in circulation, $\pm\tilde{\Gamma}_*(t)$, are plotted as error bars on each curve. These error

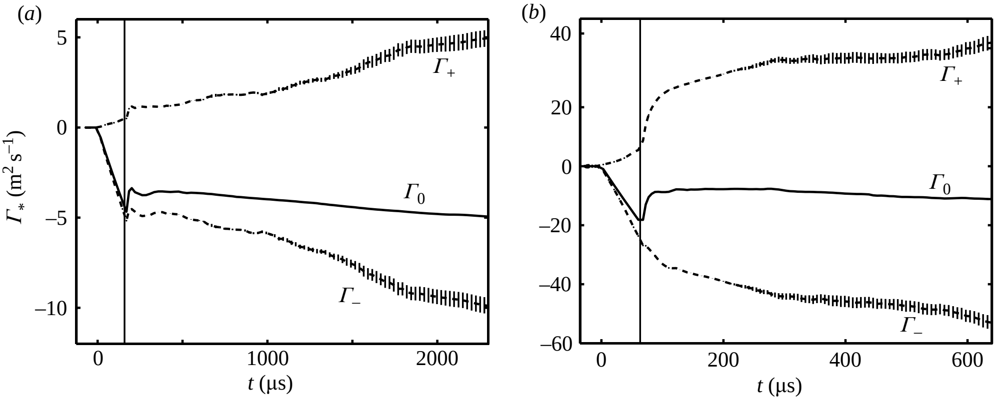

FIGURE 16. As for figure 14, but for two air–Kr scenarios: (*a*) $M = 1.2$, and (*b*) $M = 3.0$.

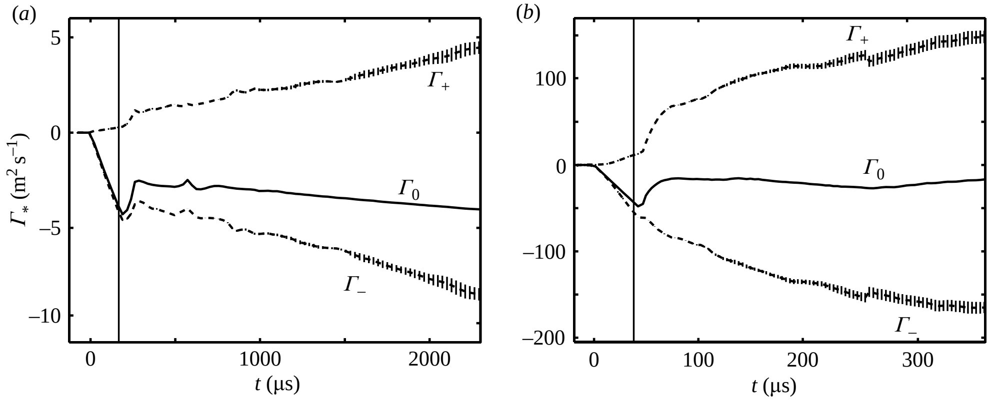

FIGURE 17. As for figure 14, but for two air–R12 scenarios: (*a*) $M = 1.13$, and (*b*) $M = 5$.

bars indicate the magnitude of azimuthal-mode fluctuations in the vortex strength, suggesting the growth of vortex bending and stretching modes in the vorticity field generated by the shock–bubble interaction.

The trends in the θ-averaged circulation show the abrupt initial shock-driven increase in primary and total circulation, followed by a 'plateau' in the total circulation. The initial rise in Γ_0 always ends near $t = t^*$; however, the 'plateau' in the total circulation does not always begin at shock passage, but later in many cases, after a period characterized by small-amplitude oscillations. Vorticity generation continues in the positive and negative components at intermediate and late times because of two effects. First, vortex-accelerated vorticity deposition (VAVD) is significant: strong vortices deposited in the flow introduce centripetal accelerations which contribute to further vortical growth. This mechanism is described in detail for Richtmyer–Meshkov instabilities by Peng *et al.* (2003), who report that the components of the circulation continue to grow even at very late times in Richtmyer–Meshkov instabilities. Secondly, vorticity generation continues owing to the reverberating scattered and diffracted shock waves and reflected rarefaction waves discussed in § 6.1 and highlighted in figure 11. Such secondary compressions and expansions generate vorticity baroclinically on the interface as they traverse the deformed bubble, causing the total circulation to continue to change in time.

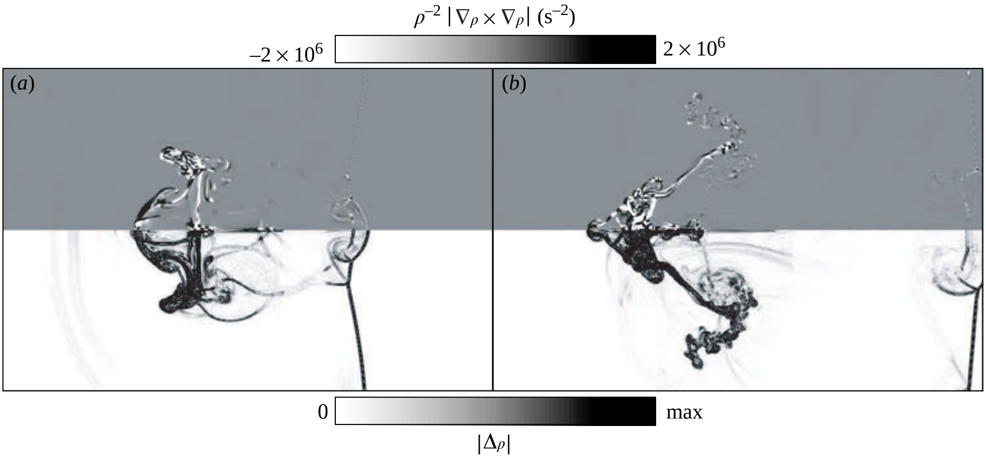

FIGURE 18. Magnitude of the baroclinic source term $\rho^{-2}\nabla\rho\times\nabla p$ (top) and Laplacian of the total density field $|\Delta\rho|$ on the $\theta=\pi/6$ slice plane, for (*a*) $t=5.0R/W^*=74.1$ µs and (*b*) $t=8.35R/W^*=123.7$ µs in the air–R12, $M=5$ scenario. Incident shock wave propagation is left-to-right.

The significance of these two effects is shown clearly in figure 18, where the magnitude of the instantaneous baroclinic source term $\rho^{-2}\nabla\rho\times\nabla p$ and the Laplacian of the density field $|\Delta\rho|$ are plotted on the $\theta=\pi/6$ slice plane, for $t=5.0R/W^*=74.1$ µs and $t=8.35R/W^*=123.7$ µs in the air–R12, $M=5$ scenario. A number of secondary shock waves are seen traversing the bubble region, and regions of continuing positive and negative baroclinic generation are visible. This is a striking example of secondary vorticity generation after the passage of the initial shock. After such secondary waves have passed out of the bubble region, indicated by $\tilde{C}(t)\rightarrow 1$ in figure 11, the components of the circulation continue to grow, by the VAVD mechanism of Peng *et al.* (2003).

The fact that Γ_+ and Γ_- continue to grow while Γ_0 remains constant at these later times indicates that the spatial distribution of vorticity decays from one dominated by a few large-scale vortices to one characterized by an increasingly large number of smaller and smaller vortex dipoles shed from the larger vortices. Such an evolution of the vorticity field is evident in the vorticity plots in figures 7 to 10, and in the corresponding movies.

For comparison with the PB, YKZ, SZ3 and one-dimensional gasdynamics-based circulation models, the circulation at the instant of shock passage is extracted from these data. The ratios of computed to modelled values of the primary net circulation at shock passage $\hat{\Gamma}_0$ are shown in figure 19, and the computed and modelled values themselves are given in table 3. The data indicate that of the four models, the SZ3 model and our proposed one-dimensional reconstruction (R) model, in general, yield the best results across the parameter space. The SZ3 model prediction, for $A>0$, has a maximum error of 22 % and an average error of 10 %. The one-dimensional reconstruction model gives a maximum error of 37 %, and an average error of 10 % across the entire parameter space, including $A<0$. In general, both models tend to overpredict the circulation slightly, though the agreement between these two models and the computed values is quite good for $A>0$, and between the R model and the computed values for $A<0$. As for the other circulation models, the YKZ model performs reliably for $A<0.2$, including the air–helium and nitrogen–argon scenarios,

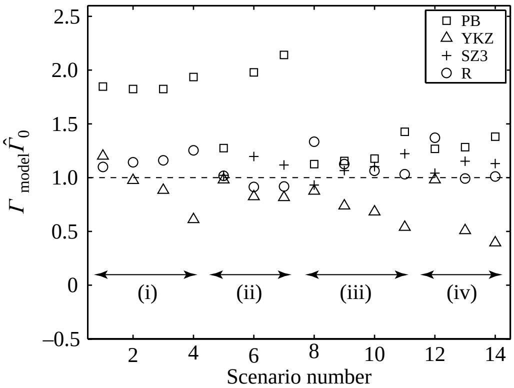

FIGURE 19. The ratio of modelled circulation to computed circulation at shock passage, $\Gamma_{model}/\hat{\Gamma}$, for each of the 14 scenarios included in this study, and all four circulation models described above. (i) Air–He, $A = -0.757$; (ii) N_2–Ar, $A = 0.176$; (iii) air–Kr, $A = 0.486$; (iv) air–R12, $A = 0.613$. See table 3 for scenario number list.

although it exhibits excessive sensitivity to the Mach number for fixed A. The PB model performs well at high density contrasts, $A > 0.2$, but overpredicts the circulation by a factor of approximately two for $A < 0$, as has been noted in PB and YKZ.

Overall, the results shown in table 3 and figure 19 suggest that a complete, predictive model for the shocked-bubble circulation does not yet exist. The SZ3 and R models provide very good estimates in general, but in sporadic cases they strongly over- or underestimate the values measured from the current simulations, and the SZ3 model is unreliable for $A < 0$. Though the R model shows good agreement with computed values within the parameter space of this study, its asymptotic properties are unknown, and its consistency can therefore not be guaranteed. Further, the two simpler models, the PB and YKZ models, which are explicitly stated to be valid only in the case of weak shock waves and small density ratios, appear to perform well in a number of cases with a high A magnitude and high M. This analysis has been performed also with circulation values measured from simulations only in regions with $f > 0$ (i.e. in the bubble fluid only), with a similar outcome. However, it is remarkable that, both in the circulation and the bubble compression and mean velocity metrics, analytical models for the shock–bubble interaction with close linkages to one-dimensional gasdynamics have performed well.

6.4. *Mixing*

Another aspect of shock–bubble interactions which is of great concern in many environments where shock-accelerated inhomogeneous flows are found is the mixing of the bubble fluid into the ambient medium. The passage of the initial shock wave over the bubble, along with all of the subsequent secondary reflected, refracted and diffracted waves, leaves a complex field of vortex lines distributed throughout the flow. This vortical field initiates vigorous mixing and the growth of turbulence-like characteristics in the flow. Although the current simulations do not resolve the dissipative length scales on which mixing takes place physically, we rely on the MILES (monotonically integrated large-eddy simulation) approach (see Fureby & Grinstein 2002) to capture the dissipative intermingling of fluids here.

Thus, a fourth integral diagnostic is applied in an attempt to characterize the intermingling of bubble fluid and ambient fluid observed in these simulations. A simple and effective means of measuring the extent of this intermingling is to compute

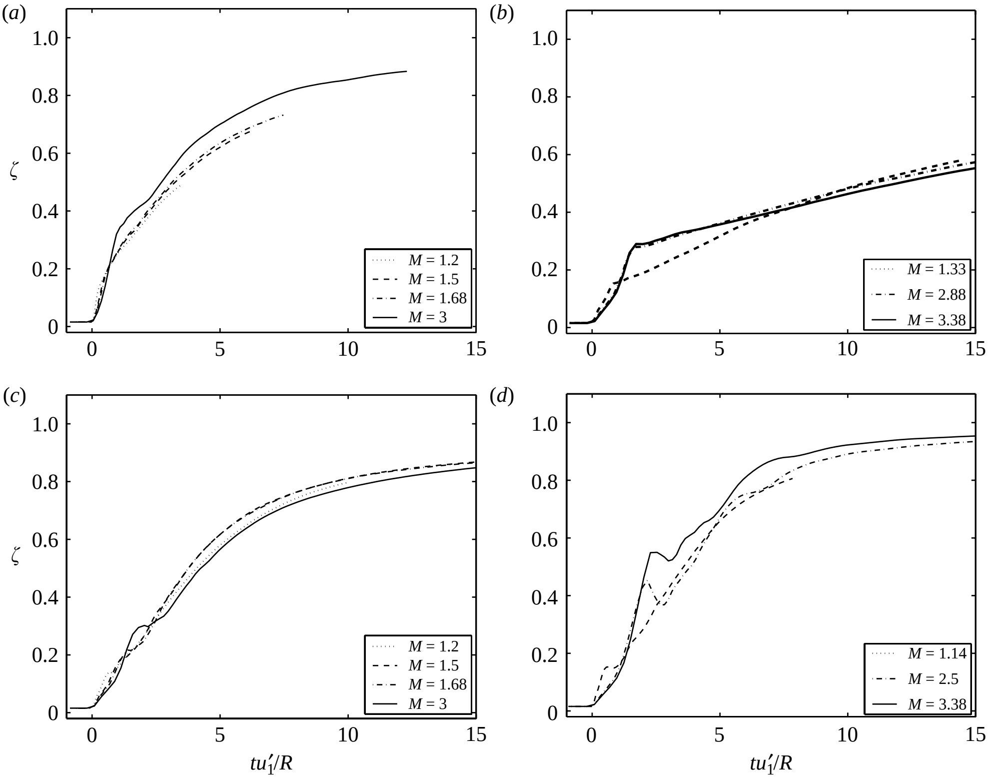

FIGURE 20. Time-dependent 'mixedness', $\zeta(t)$, obtained from three-dimensional simulations using (6.23), plotted on the dimensionless time scale tu'_1/R: (*a*) air–He, $A = -0.757$; (*b*) N_2–Ar, $A = 0.176$; (*c*) air–Kr, $A = 0.486$; and (*d*) air–R12, $A = 0.613$.

the mean volume fraction of ambient fluid in the bubble–fluid region B, where B includes all cells with $f > 0$. As the bubble is deformed by the initial shock wave and the secondary waves that interact with it, strong velocity shear and other effects draw ambient fluid into the bubble–fluid region and intermingle the two fluids. Thus, the volume fraction of fluid 2 increases and the volume fraction of fluid 1 decreases within the body of region B, and the region B grows in size. We define a 'mixedness' quantity ζ which is equivalent to the mean volume fraction of ambient fluid in the bubble–fluid region:

$$\zeta \equiv 1 - \frac{\int_B f(x, y, z, t)\, \mathrm{d}\mathscr{V}}{\int_B \mathrm{d}\mathscr{V}}. \tag{6.23}$$

This quantity characterizes the accumulated action of the process, and thus the extent to which the two fluids may be considered to have mixed.

The time-dependent 'mixedness' ζ is computed for the 14 scenarios here, and plotted in figure 20. Since the mixing behaviour is largely driven by velocity gradients in the post-shock flow, these trends are plotted on a dimensionless time scale based on u'_1 rather than W^*. The data plotted in figure 20 on this time scale collapse nearly to a single self-similar trend for each gas pairing. The mixing behaviour, computed in this way, is thus shown to depend strongly on the Atwood number, though the Mach number may be scaled out. Other time scales, based on shock-wave speeds $\tilde{W}$ or W^*, for example, did not produce the collapse seen with the u_1'-based scale for the mixing data. Thus, it is also apparent that for different quantities measured in shock–bubble interactions, different time-scaling parameters are appropriate. For the quantity ζ, u_1' is appropriate as a characteristic speed, because the rate of mixing is dependent directly on the shear rate experienced by the interface, and, thus, on the post-shock flow speed u_1'. However, as in the compression trends from § 6.1, the collapse is only successful within each gas pairing, and fails when A is varied. This is due to the nonlinear dependence of the shock scattering patterns on the initial density contrast.

As for the extent of mixing, we can see from figure 20 that the relative magnitude of ζ at late times ($tu_1'/R > 10$) grows consistently with the magnitude of A. For the nitrogen–argon scenarios, the mean ambient fluid volume fraction in the mixing region reaches a value of only about 0.6 at late times. In the higher-A cases, ζ reaches much greater values at late times: 0.8 and higher for the air–krypton cases, and 0.9 or higher for the air–R12 cases. The intensity of mixing in these scenarios is due not so much to the strength of the shock wave as to the greatly increased complexity and intensity of scattered shock waves and rarefaction waves at high A. These scattered waves also introduce non-monotonic deviations to the trends in ζ, particularly for the air–R12 cases. These are due to the gradient-steepening effects of the transit of secondary shock waves across the mixing region, which pose further obstacles to the scaling of mixing behaviour across varying A.

In the two high-M air–R12 scenarios ($M = 2.5$, 5.0), the intensity of shock refraction and vorticity generation in the shock–bubble interaction leads to the development of a large region of highly intense mixing. In this region, which is a long swath trailing downstream from the main bubble volume, the bubble fluid becomes diluted to $f < 0.1$ at very late times. Hansen *et al.* (2006) describe this behaviour, observed also in experiments, as a 'mass-stripping' process. This behaviour is distinctive for these two cases, in which, as can be seen in figure 10(*e*, *f*), the bubble is subjected to strongly focused shock waves and a series of secondary waves, and is ultimately reduced to a complex plume characterized by a large range of length scales, a complex and disorderly vorticity field and strong mixing. The volume fraction and vorticity fields from these two cases at $t = 25R/W_i$ are shown in figure 21, which clearly illustrate the high level of mixing, and indicate that the flow fields for these scenarios possess characteristics that can be described in terms of turbulence. We can assume that similar distinctive, turbulent behaviour will be observed in shock–bubble interactions when shock strengths and density contrasts are significantly large.

6.5. *Departure from axisymmetry*

The turbulent and non-axisymmetric features observed in these simulations arise because of complex shock refraction patterns and vorticity dynamics which strongly amplify initial small-scale non-axisymmetric features at high Atwood numbers. The significance of this behaviour – which is captured numerically only in three-dimensional calculations – can be characterized by measuring the enstrophy associated with non-axisymmetric components of the vorticity. In a two-dimensional axisymmetric calculation (such as those shown in § 3), the vorticity can only have a θ-component. When axisymmetry is relaxed, the vorticity may develop non-zero components in the y- (axial) and r- (radial) directions. This growth in the non-axisymmetric (y- and r-) directions is particularly strong and has significant consequences for the flow-field development when $A > 0.2$, such that the initial density contrast is significant enough to develop complex secondary shock waves.

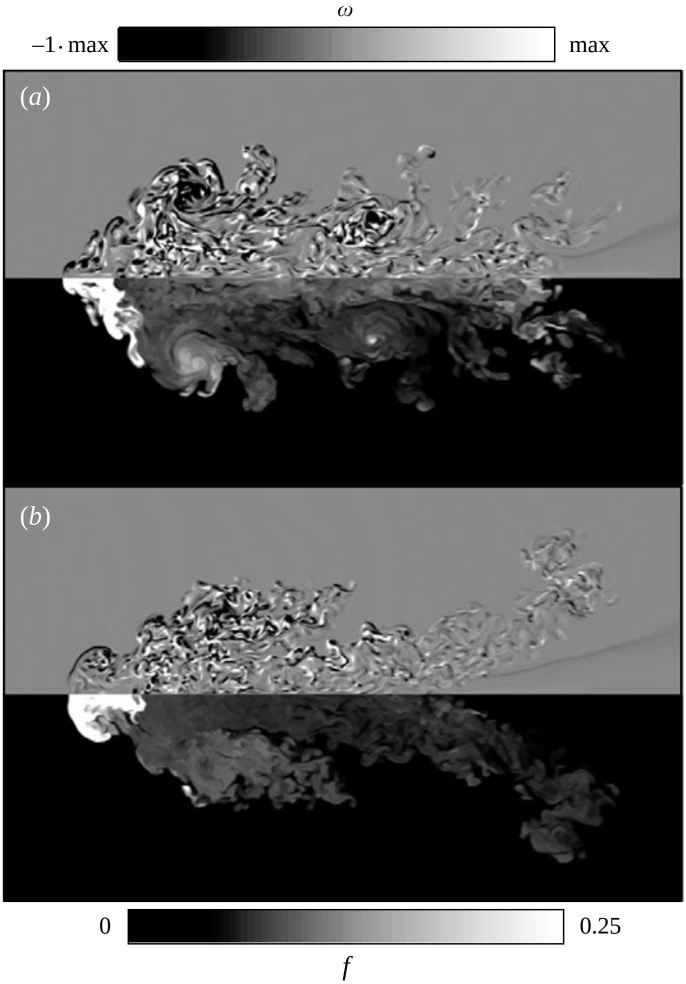

FIGURE 21. Vorticity magnitude (upper) and R12 volume fraction (lower) fields for the air–R12 scenario, at $t = 25R/W_i$, illustrating the turbulence-like flow field generated in the shock–bubble interaction at late times. (a) $M = 2.5$, (b) $M = 5.0$. Incident shock-wave propagation is from left to right.

The enstrophy associated with each component of the vorticity is therefore measured here by evaluating the integral

$$\Omega_a \equiv \int_B (\boldsymbol{\omega} \cdot \hat{a})^2 \, \mathrm{d}\mathscr{V}, \tag{6.24}$$

where $\hat{a} \in \{\hat{r}, \hat{\theta}, \hat{y}\}$. The integral is taken only over the bubble–fluid region. Trends in Ω are normalized by the value of Ω_θ at the first critical point (local maximum), and plotted as Ω' in figure 22. For $A = 0.176$, as seen in figure 22(a), the departure from axisymmetry is imperceptible, owing to the weakness of secondary shock and rarefaction waves generated in this case. From the data shown in figure 22(b) for $A = 0.613$, however, it is clear that non-axisymmetric effects are significant in the later stages of the flow-field development, even though the Mach number is lower in this case. Although the θ-component dominates at early times during the initial shock transit, and the r- and y-components are zero at that time, the departure from axisymmetry grows dramatically during the intermediate and later stages of

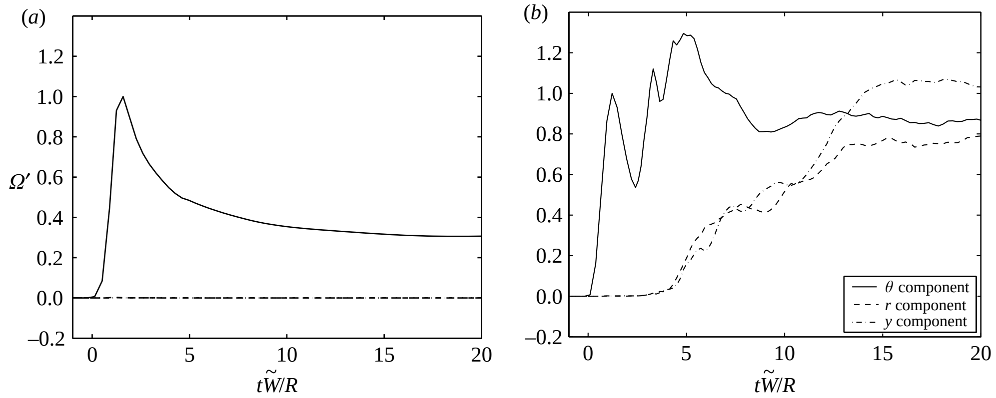

FIGURE 22. Time-dependent enstrophy associated with axisymmetric (θ-) and non-axisymmetric (r- and y-) components of the vorticity, plotted on a dimensionless time scale based on the ‘effective’ shock wave speed $\tilde{W}$: (*a*) N_2–Ar, $A = 0.176$, $M = 3.38$, (*b*) air–R12, $A = 0.613$, $M = 2.5$.

the evolution. At late times, the r- and y- components are of the same order of magnitude as the azimuthal component. This pronounced growth in the non-axisymmetric components of the vorticity accounts for the qualitative differences observed between the results of the three-dimensional air–R12 simulations shown in figures 10 and 21, and the results of the two-dimensional simulations shown in figure 4. A more complete characterization of these effects for shock–bubble interactions will require the development and applications of more effective three-dimensional diagnostics for mean and fluctuating quantities, coherent structures and mechanisms of transport and decay of turbulent features in flows such as these (see Zhang, Peng & Zabusky 2005; Niederhaus 2007), which it is anticipated will appear in future studies.

7. Conclusions

From flow-field visualizations derived from these datasets, it can be seen clearly that within the parameter space studied here, variations between the different scenarios in the behaviour of a spherical bubble subjected to a planar shock wave are large in many cases. This is apparent from the density and vorticity fields shown in figures 7 to 10. However, in spite of the apparent dissimilarities, and the strong three-dimensional and nonlinear effects arising in many cases, it is remarkable that, within each gas pairing, trends in various integral features of the flow often follow scaling laws based on one-dimensional gasdynamics analyses. The compression trends, when normalized using the value obtained by a simple one-dimensional gasdynamics analysis, and plotted on a time scale based on W^*, tend to collapse very nearly to a single curve, particularly in the lower-$|A|$ cases, including nitrogen–argon and air–krypton. At high M, however, the scaling deteriorates. Trends in the mean bubble–fluid velocity collapse to a single trend in the initial transient under a time scaling based on W_t, and are shown to approach a late-time value that is bounded by the post-shock velocities computed using one-dimensional gasdynamics. Also, the mixing trends, plotted against a time scale based on the post-shock ambient flow speed u'_1, tend to collapse nearly to a single self-similar trend.

Other properties of the shock–bubble interaction cannot yet be modelled to yield a complete successful scaling across this parameter space. This is the case for the circulation. Neither the simpler first-order models of PB and YKZ, nor the more complex SZ3 and one-dimensional-reconstruction model can predict the circulation consistently with an accuracy of better than 10%. The model introduced here, based on one-dimensional gasdynamics, however, yields the best fit to the data across this parameter space, as shown in figure 19. Successful models and scaling laws are also lacking for other aspects of the shock–bubble interaction which have not been discussed here, including in particular the bulk displacement, extent of mixing, and spatial development.

Perhaps the most remarkable result from these simulations is the complex, well-mixed plumes that result from the three-dimensional shock–bubble interaction in the two scenarios with $M > 2$ and $A > 0.5$: the air–R12 $M = 2.5$, 5.0 scenarios. In these two cases, the combined, accumulated effects of shock refraction, reflection and diffraction and intense primary and secondary vorticity generation, are so great in magnitude that the bubble region gives way to a region more appropriately characterized in terms of turbulence and disordered motion than coherent structures. It is anticipated that future simulations and post-processing diagnostic schemes, coupled with continued experimental work, will shed light on the turbulent mechanisms underlying these features.

This work was partially supported by the US Department of Energy Grant DE-FG52-06NA26196. This work was also partially performed under the auspices of the U.S. Department of Energy at the University of California, Lawrence Livermore National Laboratory under Contract No. W-7405-ENG-48.

REFERENCES

Bell, J. B., Colella, P. & Trangenstein, J. A. 1989 Higher order Godunov methods for general systems of hyperbolic conservation laws. *J. Comput. Phys.* **82**, 362–397.

Bell, J. B., Berger, M. J., Saltzman, J. S. & Welcome, M. 1994 Three dimensional adaptive mesh refinement for hyperbolic conservation laws. *SIAM J. Sci. Comput.* **15**, 127–138.

Berger, M. & Colella, P. 1989 Local adaptive mesh refinement for shock hydrodynamics. *J. Comput. Phys.* **82**, 64–84.

Berger, M. & Oliger, J. 1984 Adaptive mesh refinement for hyperbolic partial differential equations. *J. Comput. Phys.* **53**, 484–512.

Colella, P. 1985 A direct Eulerian MUSCL scheme for gas dynamics. *SIAM J. Sci. Stat. Comput.* **6**, 104–117.

Colella, P. & Glaz, H. M. 1985 Efficient solution algorithms for the Riemann problem for real gases. *J. Comput. Phys.* **59**, 264–289.

Collins, B. D. & Jacobs, J. W. 2002 PLIF flow visualization and measurements of the Richtmyer–Meshkov instability of an air/SF_6 interface. *J. Fluid Mech.* **464**, 113–136.

Crutchfield, W. Y. & Welcome, M. L. 1993 Object-oriented implementations of adaptive mesh refinement algorithms. *Sci. Prog.* **2**, 145–156.

Davy, B. A. & Blackstock, D. T. 1971 Measurements of the refraction and diffraction of a short N wave by a gas-filled soap bubble. *J. Acoust. Soc. Am.* **49**, 732–737.

Delale, C. F., Nas, S. & Tryggvason, G. 2005 Direct numerical simulations of shock propagation in bubbly liquids. *Phys. Fluids* **17**, 121705.

Fureby, C. & Grinstein, F. F. 2002 Large eddy simulation of high-Reynolds-number free and wall-bounded flows. *J. Comput. Phys.* **181**, 68–97.

Giordano, J. & Burtschell, Y. 2006 Richtmyer–Meshkov instability induced by shock–bubble interaction: numerical and analytical studies with experimental validation. *Phys. Fluids* **18**, 036102.

GORDON, S. & MCBRIDE, B. J. 1976 Computer program for computation of complex chemical equilibrium compositions, rocket performance, incident and reflected shocks, and Chapman–Jouguet detonations. Spec. Publ. SP-273. Lewis Research Center, NASA.

GREENOUGH, J. A., BECKNER, V., PEMBER, R. B., CRUTCHFIELD, W. Y., BELL, J. B. & COLELLA, P. 1995 An adaptive multifluid interface-capturing method for compressible flow in complex geometries. *AIAA Paper* 95-1718.

GREENOUGH, J. A., DE SUPINSKI, B., YATES, R. K., RENDLEMAN, C. A., SKINNER, D., BECKNER, V. E., LIJEWSKI, M. & BELL, J. B. 2005 Performance of a block structured hierarchical adaptive mesh refinement code on the 64K node IBM BlueGene/L computer. *LBNL Rep.* LBNL-57500. Lawrence Berkeley National Laboratory, Berkeley, CA.

HAAS, J.-F. & STURTEVANT, B. 1987 Interaction of weak shock waves with cylindrical and spherical inhomogeneities. *J. Fluid Mech.* **181**, 41–76.

HANSEN, J. F., ROBEY, H. F., KLEIN, R. I. & MILES, A. R. 2006 Mass-stripping analysis of an interstellar cloud by a supernova shock. *Astrophys. Space Sci.* Online version.

HENDERSON, L. F. 1966 The refraction of a plane shock wave at a gas interface. *J. Fluid Mech.* **26**, 607–637.

HENDERSON, L. F. 1989 On the refraction of shock waves. *J. Fluid Mech.* **198**, 365–386.

HENDERSON, L. F., COLELLA, P. & PUCKETT, E. G. 1991 On the refraction of shock waves at a slow–fast gas interface. *J. Fluid Mech.* **224**, 1–27.

JACOBS, J. W. 1993 The dynamics of shock accelerated light and heavy gas cylinders. *Phys. Fluids* A **5**, 1993.

JAMALUDDIN, A. R., BALL, G. J. & LEIGHTON, T. J. 2005 Free-Lagrange simulations of shock/bubble interaction in shock wave lithotripsy. In *Shock Waves: Proc. 24th Intl Symp. on Shock Waves* (ed. Z. L. Jiang).

KLEIN, R. I., MCKEE, C. F. & COLELLA, P. 1994 On the hydrodynamic interaction of shock waves with interstellar clouds. I. Nonradiative shocks in small clouds. *Astrophys. J.* **420**, 213–236.

KLEIN, R. I., BUDIL, K. S., PERRY, T. S. & BACH, D. R. 2003 The interaction of supernova remnants with interstellar clouds: experiments on the NOVA laser. *Astrophys. J.* **583**, 245–259.

LATINI, M., SCHILLING, O. & DON, W. S. 2006 Effects of WENO flux reconstruction order and spatial resolution on reshocked two-dimensional Richtmyer–Meshkov instability. *J. Comput. Phys.* **221**, 805–836.

LAYES, G. 2005 Etude expérimentale de l'interaction d'une onde de choc avec une bulle de gaz. PhD thesis, Université de Provence (Aix-Marseille I).

LAYES, G., JOURDAN, G. & HOUAS, L. 2003 Distortion of a spherical gaseous interface accelerated by a plane shock wave. *Phys. Rev. Lett.* **91** (17).

LAYES, G., JOURDAN, G. & HOUAS, L. 2005 Experimental investigation of the shock wave interaction with a spherical gas inhomogeneity. *Phys. Fluids* **17**, 028103.

LAYES, G. & LEMÉTAYER, O. 2007 Quantitative numerical and experimental studies of the shock accelerated heterogeneous bubbles motion. *Phys. Fluids* **19**, 042105.

LEE, D.-K., PENG, G. & ZABUSKY, N. J. 2006 Circulation rate of change: a vortex approach for understanding accelerated inhomogeneous flows through intermediate times. *Phys. Fluids* **18**, 097102.

VAN LEER, B. 1979 Towards the ultimate conservative difference scheme. *J. Comput. Phys.* **32**, 101–136.

LIEPMANN, H. W. & ROSHKO, A. 1957 *Elements of Gasdynamics*. John Wiley.

LINDL, J. 1995 Development of the indirect-drive approach to inertial confinement fusion and the target physics basis for ignition and gain. *Phys. Plasmas* **2**, 3933–4024.

MARQUINA, A. & MULET, P. 2003 A flux-split algorithm applied to conservative models for multicomponent compressible flows. *J. Comput. Phys.* **185**, 120–138.

MESHKOV, YE. YE. 1970 Instability of a shock wave accelerated interface between two gases. *NASA TT* F-13074.

MILLER, G. H. & PUCKETT, E. G. 1996 A higher-order Godunov method for multiple condensed phases. *J. Comput. Phys.* **128**, 134–164.

NIEDERHAUS, J. H. J. 2007 A computational parameter study for three-dimensional shock–bubble interactions. PhD thesis, University of Wisconsin-Madison.

Peng, G., Zabusky, N. J. & Zhang, S. 2003 Vortex-accelerated secondary baroclinic vorticity deposition and late-intermediate time dynamics of a two-dimensional Richtmyer–Meshkov interface. *Phys. Fluids* **15**, 3730–3744.

Picone, J. M. & Boris, J. P. 1988 Vorticity generation by shock propagation through bubbles in a gas. *J. Fluid Mech.* **189**, 23–51.

Picone, J. M., Oran, E. S., Boris, J. P. & Young Jr, T. R. 1985 Theory of vortiity generation by shock wave and flame interactions. In *Dynamics of Shock Waves, Explosions, and Detonations* (ed. J. R. Bowen, N. Manson, A. K. Oppenheim & R. I. Soloukhin), *Progress in Astronautics and Aeronautics*, vol. 94, chap. 4, pp. 429–448. AIAA.

Pope, S. B. 2000 *Turbulent Flows*. Cambridge University Press.

Quirk, J. J. & Karni, S. 1996 On the dynamics of a shock–bubble interaction. *J. Fluid Mech.* **318**, 129–163.

Ranjan, D., Anderson, M., Oakley, J. & Bonazza, R. 2005 Experimental investigation of a strongly shocked gas bubble. *Phys. Rev. Lett.* **94**, 184507.

Ranjan, D., Niederhaus, J., Motl, B., Anderson, M., Oakley, J. & Bonazza, R. 2007 Experimental investigation of primary and secondary features in high-Mach-number shock–bubble interaction. *Phys. Rev. Lett.* **98**, 024502.

Ray, J., Samtaney, R. & Zabusky, N. J. 2000 Shock interactions with heavy gaseous elliptic cylinders: two leeward-side shock competition modes and a heuristic model for interfacial circulation deposition at early times. *Phys. Fluids* **12**, 707–716.

Rendleman, C. A., Beckner, V. E., Lijewski, M., Crutchfield, W. Y. & Bell, J. B. 1998 Parallelization of structured, hierarchical adaptive mesh refinement algorithms. *Comput. Visualiz. Sci.* **3**, 147–157.

Richtmyer, R. D. 1960 Taylor instability in shock accleration of compressible fluids. *Commun. Pure Appl. Maths* **13**, 297–319.

Rudinger, G. & Somers, L. M. 1960 Behaviour of small regions of different gases carried in accelerated gas flows. *J. Fluid Mech.* **7**, 161–176.

Samtaney, R. & Pullin, D. I. 1996 On initial-value and self-similar solutions of the compressible Euler equations. *Phys. Fluids* **8**, 2650–2655.

Samtaney, R., Ray, J. & Zabusky, N. J. 1998 Baroclinic circulation generation on shock accelerated slow/fast gas interfaces. *Phys. Fluids* **10**, 1217–1230.

Samtaney, R. & Zabusky, N. J. 1994 Circulation deposition on shock-accelerated planar and curved density-stratified interfaces: models and scaling laws. *J. Fluid Mech.* **269**, 45–78.

Strang, G. 1968 On the construction and comparison of different schemes. *SIAM J. Numer. Anal.* **5**, 506–517.

Widnall, S. E., Bliss, D. B. & Tsai, C. Y. 1974 The instability of short waves on a vortex ring. *J. Fluid Mech.* **66**, 35–47.

Winkler, K.-H., Chalmers, J. W., Hodson, S. W., Woodward, P. R. & Zabusky, N. J. 1987 A numerical laboratory. *Phys. Today* **40** (10), 28–37.

Yang, J., Kubota, T. & Zukoski, E. E. 1994 A model for characterization of a vortex pair formed by shock passage over a light-gas inhomogeneity. *J. Fluid Mech.* **258**, 217–244.

Zabusky, N. J. 1999 Vortex paradigm for accelerated inhomogeneous flows: visiometrics for the Rayleigh–Taylor and Richtmyer–Meshkov environments. *Annu. Rev. Fluid Mech.* **31**, 495–536.

Zabusky, N. J. & Zeng, S. M. 1998 Shock cavity implosion morphologies and vortical projectile generation in axisymmetric shock-spherical fast/slow bubble interactions. *J. Fluid Mech.* **362**, 327–346.

Zhang, S., Peng, G. & Zabusky, N. J. 2005 Vortex dynamics and baroclinically forced inhomogeneous turbulence for shock-planar heavy curtain interactions. *J. Turbulence* **6**, 1–29.